Encelascope Navigation Final Report

Prepared by:
Advanced Space, LLC
1400 W 122nd Avenue, Suite 200
Westminster, CO 80234
Phone: 720-545-9191
Home Page: www.advancedspace.com

August 8, 2022

Table of Contents

Executive Summary

This report presents navigation analyses which support the effort to determine feasibility of a low-cost interplanetary satellite mission to Enceladus for the ASTROBi Foundation. The primary constraint placed on the navigation strategy for this mission is to limit the use of ground-based radiometric observables to save on mission operations costs. The primary navigation strategy under consideration is Line of Sight (LOS) optical navigation. The analyses presented here apply this optical navigation strategy to each phase of the mission and evaluate expected navigation uncertainty under varying optical and operational conditions throughout the mission. Additionally, analysis of the less common, but promising use of a star occultation timing navigation strategy in the science orbit at Enceladus is presented. In addition to focusing on optical navigation strategies, critical events in the mission timeline such as planetary flybys and deep-space maneuvers have been analyzed additionally with supplemental radiometric navigation observables with varying observable quality and tracking cadence to support future higher-fidelity cost and mission risk analyses surrounding these events. Assessment of the results indicate that an optical navigation strategy supplemented with radiometric navigation observables could prove reliable for this mission, with some caveats surrounding critical events and some regimes of the trajectory. However, further analysis which includes the effects of these navigation errors on trajectory and maneuver optimization must be performed to fully validate optical navigation for this mission.

This analysis was performed by Advanced Space in support of and with funding from the ASTROBi Foundation. Additional analyses were performed studying the mission design and ground system for this mission, which are summarized in independent reports.

Technical Activities

Optical Navigation Summary

Simulation Setup

Navigation studies are performed using MONTE, an astrodynamics toolkit designed by NASA's Jet Propulsion Laboratory capable of general-purpose orbit calculations, trajectory optimization, and orbit determination. MONTE is currently used by Advanced Space to navigate CAPSTONE to the Moon and has been used for nearly every JPL-navigated mission since 2012 [1].

The orbit determination studies presented here utilize MONTE's implementation of a Conventional Kalman Filter. Trajectories are studied one "leg" at a time. A leg of the trajectory refers to the spacecraft's trajectory between two planet or satellite flybys. Each leg of the trajectory is analyzed by first simulating measurements calculated using trajectory products from the mission design team. The measurements are then processed in the filter as a covariance study. A covariance study is similar to a normal implementation of a filter but skips any updates to estimated parameters and only processes updates to estimated uncertainty. Because the tools and dynamics used for mission design and orbit determination disagree slightly, pure filter studies are hindered and can potentially diverge – skewing results in the process. Filter scenarios are run as covariance studies to capture estimated uncertainty evolution without the need for high-fidelity filter design. More

detail on the dynamics and measurement models used for these studies can be found in the *Dynamical Models* and *Measurement Models* sections, respectively.

The filter is configured to report uncertainty of the spacecraft state in a J2000 inertially-fixed frame using cartesian coordinates as well as uncertainty projected forward the next flyby for any given leg of the trajectory using B-Plane coordinates. The B-Plane is a hypothetical plane that a spacecraft would pass perpendicularly through if it were unaffected by the gravity force of the target flyby body. This parameterization of target body intercept linearizes much of what is otherwise a highly nonlinear dynamical encounter. Figure 1 shows an example illustration of the B-Plane. The location of a flyby encounter on the T and R axes of this plane yields predictable behavior for the actual nonlinear effects of performing a flyby without needing to analyze a full 6-dimensional orbit state.

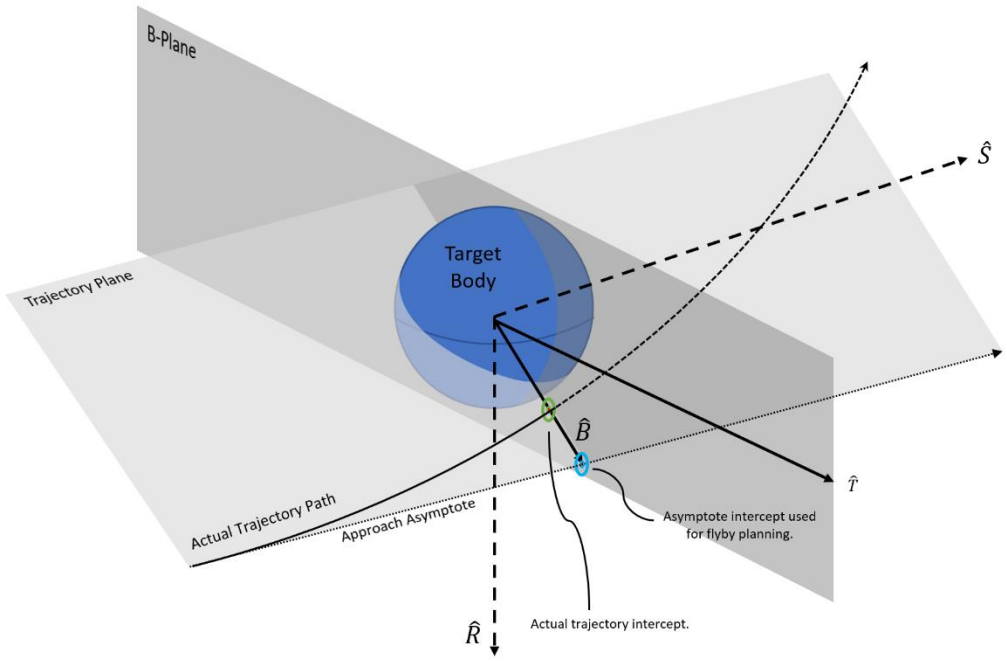

Figure 1: Illustration of the B-Plane. B-Plane coordinates are parameterized along the R and T directions, perpendicular to the approach asymptote. Diagram adapted from [2].

Dynamical Model

The navigation filter propagates the spacecraft state using point mass gravity from the Sun and barycenters[1] of Mercury, Venus, Earth, Mars, Jupiter, Saturn (while outside the Saturnian sphere of influence), Uranus, Neptune, and Pluto. Maneuvers are implemented as impulsive burns. Internal to the Saturnian sphere of influence (SOI), the gravitational influence of Saturn itself and its satellites: Titan, Rhea, Dione, Tethys, and Enceladus are included in trajectory propagation. Ephemeris data is drawn from DE430 for planets and SAT375 made available by the Jet Propulsion Laboratory.

[1] Gravity force modelled using the total mass of and originating from planet-moon system barycenter when spacecraft is far from individual gravitational bodies relative to the bodies' spheres of influence.

Measurement Models

Inertial Angle Measurements of Solar System Bodies

During the interplanetary and Saturn moon tour phases of the mission, measurements of the line-of-sight (LOS) direction from the spacecraft to Solar System bodies, or beacons, are used as the primary orbit determination observable. Practically, these measurements are derived from images of planets, moons, and asteroids taken onboard the spacecraft. The starfield in the background of these images is used to solve for the attitude of the camera boresight. The direction to the imaged beacon can then be determined based on its location within the image [3]. The studies presented here assume image processing for determining camera direction from a starfield and recognizing and locating a beacon within the image can determine the direction to the body to within 6 arcseconds 1-sigma. This level of measurement precision is consistent with current technology [4]. Raw measurements are simulated as right ascension (RA) and declination (Dec) values oriented in a spacecraft centered J2000 frame and overlaid with 6 arcsec 1σ STD white noise. Figure 2 diagrams the geometry of this problem.

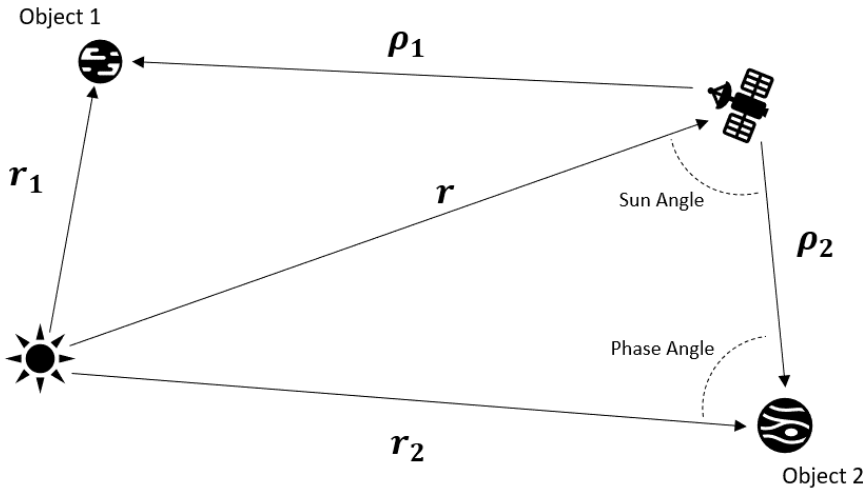

Figure 2: Line-of-sight optical navigation problem. Given known r_1 and r_2, measured directions of $\rho_1$and ρ_2, r, the spacecraft's inertial position, can be solved algebraically. Adapted from [5].

The visibility of measurements is constrained by beacon brightness, a function of phase angle, and beacon-spacecraft-Sun angle, or Sun angle. Beacon brightness is evaluated using empirical models for visual magnitude which derives visual magnitude of a body from its absolute magnitude, V(1,0), solar phase law, m, (as a function of phase angle) distance between the spacecraft and body, ρ, and the distance between the body and the Sun, r_b. The following equation describes the full model for visual magnitude of the body as seen from the spacecraft [6].

$$V = V(1,0) + 5log_{10}(\rho r_b) + m$$

The beacons used during the interplanetary study are denoted in Table 1 along with relevant brightness parameters [6]. Measurements are simulated only if the calculated visual magnitude is lower than 6.0. The limiting visual magnitude for an imager can vary greatly with cost. The value chosen here corresponds with a low- to middle-grade imager [4].

Table 1: Absolute magnitude and phase law as a function of phase angle for target beacon bodies during interplanetary cruise.

Body	Absolute magnitude and phase law (m) as a function of phase angle (α) in degrees.	
	V(1,0)	m
Mercury	-0.36	$0.038\ \alpha - 2.73(\alpha/100)^2 + 2.00(\alpha/100)^3$
Venus	-4.29	$0.009\ \alpha + 2.39(\alpha/100)^2 - 0.65(\alpha/100)^3$
Earth	-3.86	$0.016\ \alpha$
Mars	-1.52	$+ 0.016\ \alpha$
Jupiter	-9.25	$+ 0.005\ \alpha$
Saturn[2]	-8.90	$+ 0.044\ \alpha$

An example showing how beacon viewability affects the ability of the spacecraft to gather measurements is shown in Figure 3 and Figure 4 for the first Earth-Venus leg of the interplanetary trajectory. Note that visual magnitude of all beacons stays below 6.0 for the duration of the leg, so it does not constrain the viewability of beacons for this study. The Sun angle of beacons relative to the spacecraft is far more constraining, limiting viewability of Mercury for most of the leg and limiting viewability of other beacons intermittently throughout the trajectory.

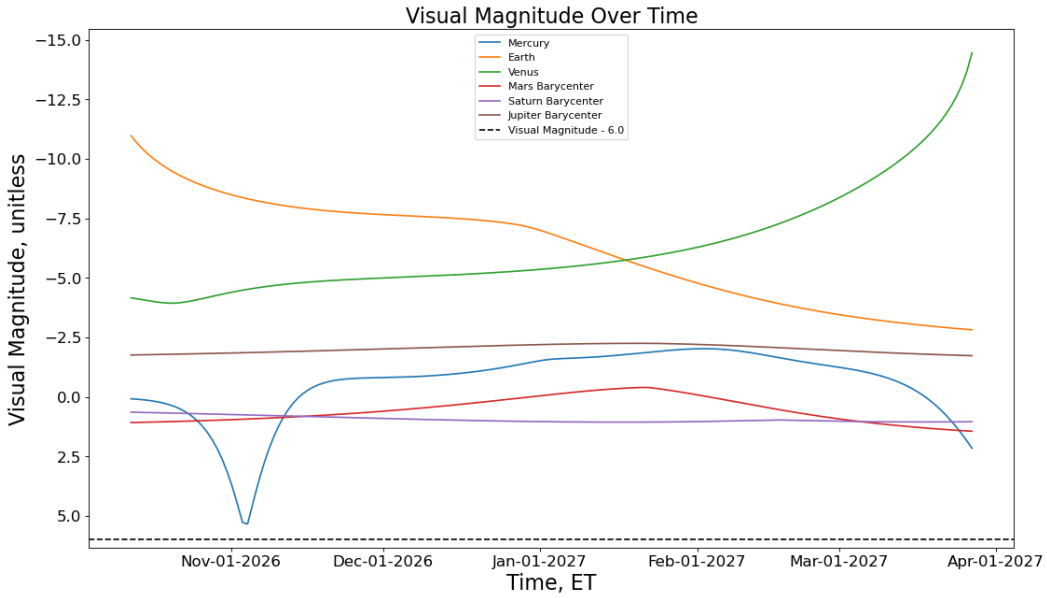

Figure 3: Visual magnitude of beacons as viewed from the spacecraft between launch and the first Venus flyby. All beacons remain bright enough for a standard imager to capture.

[2] Note that this model does not take the perspective of Saturn's rings into account. However, as a check for whether Saturn can be seen at all, rather than modelling apparent brightness as a measurement observable, the model provided will suffice.

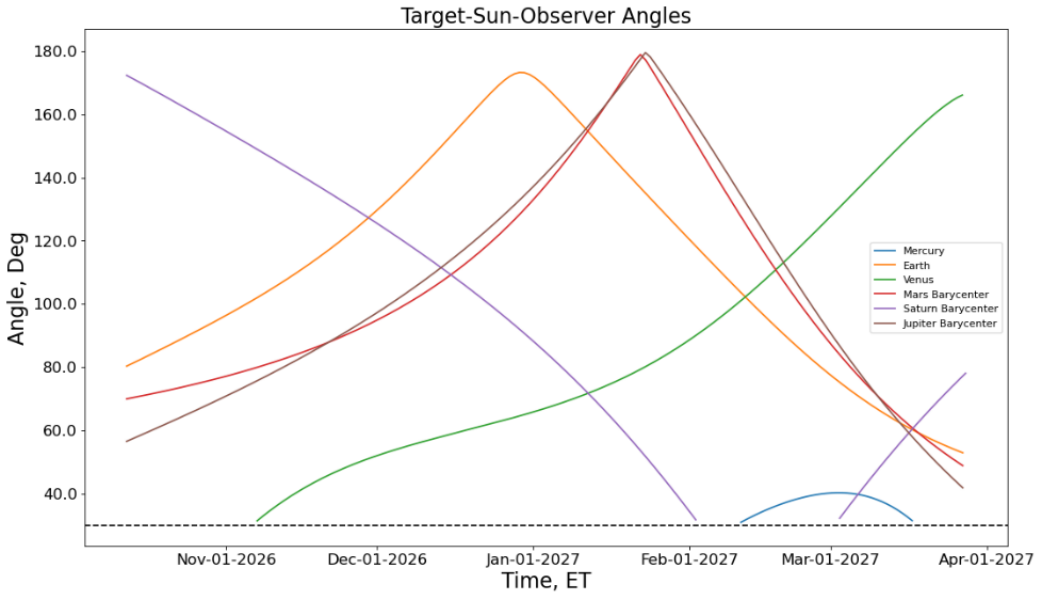

Figure 4: Sun angles for all beacons between launch and the first Venus flyby. Mercury stays within 30 degrees of the Sun for most of the leg.

In addition to beacon viewability, aconstraint can be made to choose an optimal pair of beacons at any given time in the trajectory. This is especially useful for a spacecraft with operational constraints which would restrict it from freely imaging all viewable beacons. For example, collecting and downlinking science data or executing a long low-thrust maneuver limit the time available for gathering navigation observables [6]. Optimal beacon pairs can be chosen using a figure of merit derived from the uncertainty in a state estimate using a batch least squares solution. The derivation for the figure of merit can be found in [5]. The main elements of the LOS optical navigation problem which feed into the figure of merit are the beacon-spacecraft-beacon angle and the relative distance between the spacecraft and each beacon in a candidate pair. This metric favors close beacons whose position vectors relative to the spacecraft form a near 90-degree angle. Because the current iteration of the spacecraft trajectory contains no low-thrust maneuvers and an overarching goal of the mission is to limit ground contact time, during the interplanetary and moon tour phases of the mission the spacecraft ability to gather measurements of beacons should not be significantly limited, and these analyses utilize all viewable beacons throughout the trajectory.

A final constraint which has not been modeled for these analyses is the operational plan for slewing the spacecraft between imaging attitudes. For these analyses, measurements are simulated simultaneously for each viewable beacon at every imaging time, which is fixed to a 5 minute imaging cadence. A summary of measurement simulation constraints and parameters are denoted in Table 2.

Table 2: Summary of optical measurement simulation parameters.

Parameter	Value
Measurement Noise	6 arcsec - 1σ
Visual Magnitude	< 6.0
Sun angle	> 30 deg

Imaging cadence	5 minutes

Ground-Based Radiometric Measurements

In analysis case where optical navigation is supplemented by ground-based radiometric tracking, range and range-rate (Doppler) measurements are simulated using Deep Space Network (DSN) stations. To account for limited DSN usage, measurements are simulated with varying noise values and tracking schedules to emulate radiometric tracking from lower quality ground stations. These details are listed in Table 6.

Additional Sources of Uncertainty

Additional sources of uncertainty are included in these studies to provide more realistic estimates of spacecraft state uncertainty. These sources include uncertainty in the gravitational parameters of Solar System bodies, uncertainty due to random mismodelled dynamics, and trajectory correction maneuver errors. These sources and their corresponding uncertainties can be found in Table 3. It should be noted that maneuver execution errors are system-specific while all other sources of uncertainty listed here are system-agnostic. For chemical propulsion systems, maneuver delta-V errors generally include a fixed and proportional component. Proportional errors scale with maneuver magnitude, while fixed errors do not. Fixed maneuver delta-V errors are generally much less significant than the proportional errors and have not been included here. Pointing errors are implemented as a fixed error distribution based on assumed spacecraft's attitude capabilities. 1%-1 sigma proportional delta-V magnitude errors and 1° -1 sigma pointing errors are typical for spacecraft with chemical propulsion systems capable of performing 10s to 100s of m/s maneuvers, which matches the maneuver profile for this mission.

Table 3: Additional sources of uncertainty and their magnitudes.

Uncertainty Source	Uncertainty (1-sigma)
Impulsive Maneuver Magnitude	1% of total DV
Impulsive Maneuver Direction	1°
Sun Gravitational Parameter (GM)	10. km^3/s^2
Mercury GM	1.4 km^3/s^2
Venus GM	6.4e-3 km^3/s^2
Earth GM	8.0e-4 km^3/s^2
Moon GM	1.4e-5 km^3/s^2
Mars Barycenter GM	2.8e-4 km^3/s^2
Jupiter Barycenter GM	2.1 km^3/s^2
Saturn Barycenter GM	1.1 km^3/s^2
Uranus Barycenter GM	7.6 km^3/s^2
Neptune Barycenter GM	11. km^3/s^2
Pluto Barycenter GM	0.2 km^3/s^2
Random unmodelled accelerations	1.0e-11 km/s^2

Optical Navigation Studies

Interplanetary Trajectory Studies

Optical-only Navigation

The feasibility of optical-only navigation during the interplanetary EVVES cruise requires that optical right ascension (RA) and declination (DEC) measurements of planetary beacons with respect to the spacecraft are sufficient to provide knowledge of the spacecraft's state such that trajectory predictions can confidently be used to coordinate correction maneuvers and safely navigate planetary flybys. The navigational analyses for the interplanetary cruise and Saturnian moon tour assume a consistent measurement flow at a cadence of one measurement per beacon every 5 minutes. This consistent measurement flow when spanned over a long trajectory arc, one which allows for significant change in the right ascension and declination measurements with respect to the measured planetary beacons, allows for a tight constraint on the position and velocity of the spacecraft, without the inclusion of uncertainty on the location of the planetary beacons.

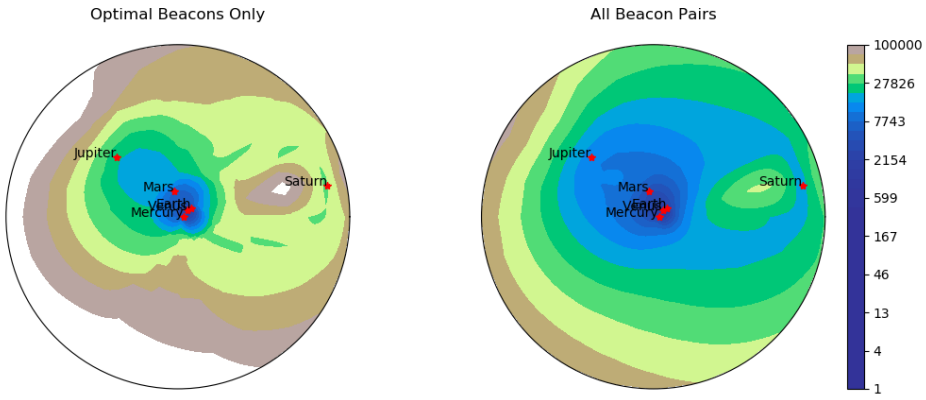

Figure 5: 1-sigma variance of spacecraft positional state uncertainty under measurement configurations which include only the optimal pair of planetary beacons (left) and all available planetary beacons (right). Uncertainty metric and methods from [4].

Generally, right ascension and declination measurements to the planetary beacons (being: Mercury, Venus, Earth, Mars, Jupiter, and Saturn) provide positional state knowledge during deep-space travel in the inner solar system consistent with approximately 100-300km 3-sigma, and velocity state knowledge between 10cm/s and 1 m/s. Localized decreases in state uncertainty are seen in close proximity to a planetary beacon, where the relative motion between the spacecraft and the beacon becomes more observable over shorter timespans. Moreover, solar exclusion (when the available beacons have too low an angular difference with respect to the Sun) serves to worsen the discernable position knowledge late in the interplanetary cruise while outbound to the Saturnian system, when most of the available planetary beacons are too close to the Sun to be observed. Additionally, during interplanetary cruise, where the relative motion between the spacecraft and beacons is less pronounced, the state solution worsens.

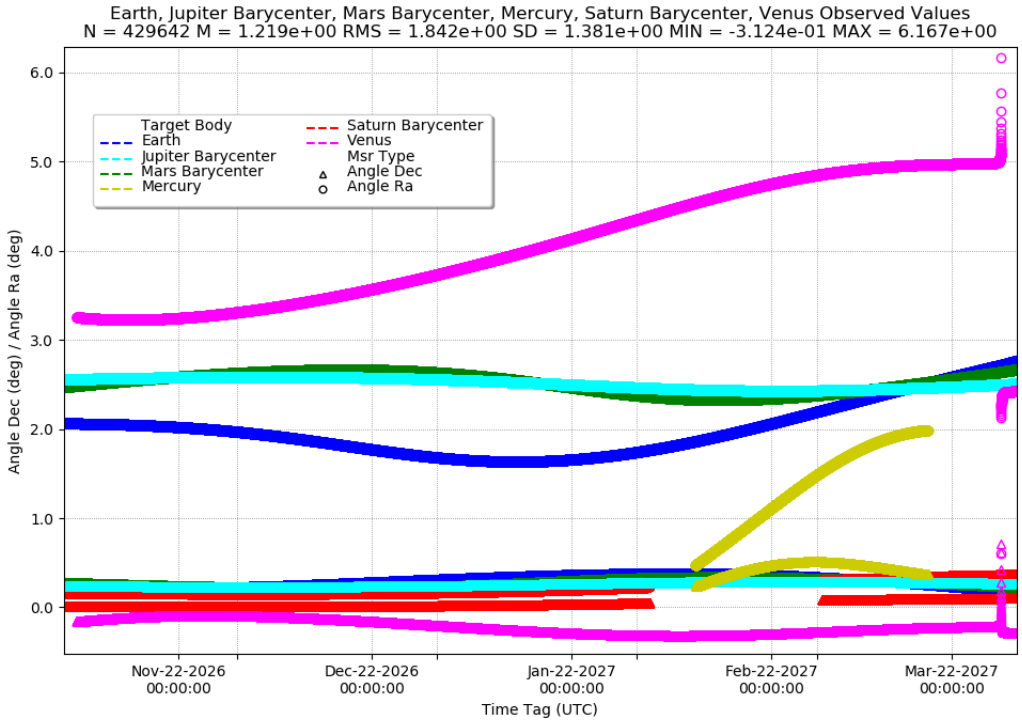

Figure 6: Right ascension and declination measurements collected during the Earth-Venus trajectory leg

Figure 6 presents the set of right ascension and declination measurements collected during the first Earth-Venus trajectory leg. The planetary beacons with the largest variability in right ascension are Earth and Venus, with rapid variability in the Venus right ascension measurements surrounding the Venus flyby, seen on the right. This suggests that during interplanetary travel, the information content of the observed measurements varies by relatively small amounts over short durations, except when approaching the upcoming flyby body. It can therefore be inferred that longer measurement arcs are required to constrain the state uncertainty to an appropriate size during cruise and between flybys – a diversity in inertial viewing geometry to each beacon is much more important than the short-term sampling rate of the measurement type.

The interplanetary cruise is analyzed on an arc-by-arc basis, each arc spanning a trajectory leg between planets. The navigation analysis for the interplanetary cruise is therefore split into four arcs:

Table 4: Interplanetary cruise launch, flyby, and arrival dates

Trajectory Leg	Start Date	End Date
Earth-Venus	05-OCT-2026 05:55:41 TDB	29-MAR-2027 14:00:34 TDB
Venus-Venus	29-MAR-2027 14:00:34 TDB	20-JUN-2028 21:09:57 TDB
Venus-Earth	20-JUN-2028 21:09:57 TDB	21-SEP-2030 11:06:07 TDB
Earth-Saturn	21-SEP-2030 11:06:07 TDB	12-NOV-2035 18:26:02 TDB

Each arc is analyzed independently, where right ascension and declination measurements acquired during a given arc are used to estimate the state uncertainty along that arc. Subsequently, B-plane crossing predictions and their associated uncertainties are made along each arc, where the

instantaneous state uncertainty at a given time is used to make a prediction of the conditions at the upcoming flyby, as well as the uncertainty associated with that B-plane prediction. Included in this analysis are statistical trajectory correction maneuvers (TCMs) and deterministic deep space maneuvers (DSMs). All maneuvers are implemented with a magnitude uncertainty of 1% 1σ and pointing error of 1° 1σ. For the reported covariance analysis, statistical TCMs impart no change in velocity; they only serve to inflate the spacecraft's velocity uncertainty, and function as a placeholder for the approximate size and location of a maneuver which may be necessary en-route to the next flyby.The DSMs used are pulled from trajectory design products, and do impart a change to the spacecraft's velocity, as they are required for modeling the spacecraft's trajectory to the next flyby. En-route maneuvers for the interplanetary legs are implemented as follows:

Table 5: Deterministic and statistical maneuvers implemented in the interplanetary cruise covariance analysis

Deterministic Deep Space Maneuvers (DSMs)			
Trajectory Leg	**TCM Location**	**TCM Magnitude**	**Error 1σ**
Earth-Venus	31-JAN-2027 12:18:12 TDB	5.311 m/s	1%, 1°
Venus-Venus	18-NOV-2027 09:55:42 TDB	1.177 m/s	1%, 1°
Earth-Saturn	21-SEP-2030 12:49:19 TDB	310.456 m/s	1%, 1°
Earth-Saturn	13-FEB-2033 16:51:06 TDB	38.513 m/s	1%, 1°
Statistical Trajectory Correction Maneuvers (TCMs)			
Trajectory Leg	**TCM Location**	**TCM Magnitude**	**Error 1σ**
All	T_0 + 21 days	20 m/s	1%, 1°
All	Mid-cruise	5 m/s	1%, 1°
All	T_f – 21 days	1 m/s	1%, 1°
All	T_f – 7 days	0.1 m/s	1%, 1°

TCMs are assumed to be executed relative to the start and end of the arcs between flybys: 21 days after launch or flyby to clean up flyby execution errors, a mid-cruise trajectory correction, and two B-plane targeting TCMs executed 21 days and 7 days prior to an upcoming flyby. Below, an example is given which showcases the initial Earth-Venus leg uncertainty evolution under the statistical TCM and deterministic DSM configuration noted in Table 5. This illustrates a case where an additional post-launch cleanup TCM is implemented alongside the nominal four statistical TCMs and deterministic DSM on Jan 31st, 2027.

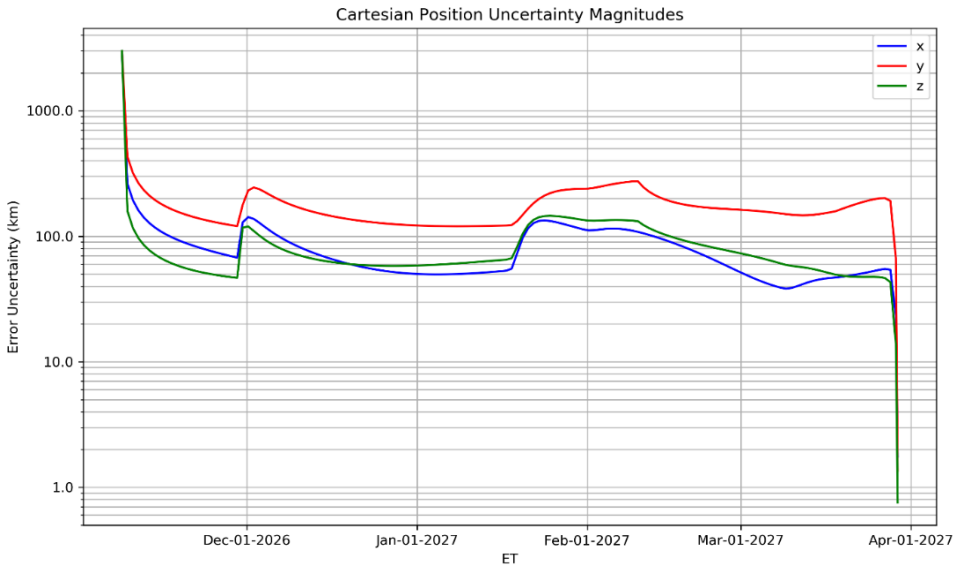

Figure 7: 3σ positional uncertainty along the first Earth-Venus arc, shown on a log scale

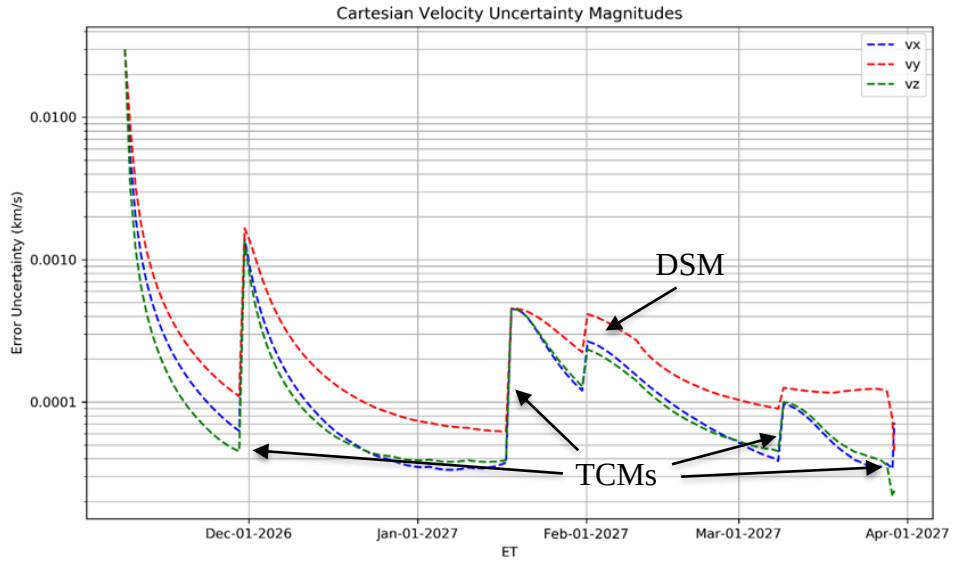

Figure 8: 3σ velocity uncertainty along the first Earth-Venus arc, shown on a log scale

Here, the trajectory's response to increases in the velocity uncertainty is directly observable in Figure 8, where the deterministic DSM and statistical TCMs are responsible for the sharp increases in velocity uncertainty. The response takes weeks to settle back to the previous steady state, and the average 3σ velocity uncertainty is maintained between 0.1 and 1 m/s. The response is visible in Figure 7 as well, showing that an increase in velocity uncertainty is matched by a corresponding growth in positional uncertainty, as the time rate of change of positional uncertainty is related to the size of the velocity uncertainty. Additionally, a sharp decrease in positional uncertainty is noted at the end of the arc, denoting the rapid approach to Venus, where the relative motion of the spacecraft with respect to Venus serves to constrain the possible positional states which may produce the measurements shown in Figure 6. The state estimate and corresponding uncertainty along the arc may be used to predict the upcoming B-plane crossing conditions and accompanying uncertainty for the first Venus flyby. It is noted that, for a time during the flyby, Venus cannot be

used as an imaging beacon because the planet will fill the frame of the camera, or at least obscure enough stars that an attitude solution cannot be determined from the starfield. The time span in which this occurs is camera-dependent, so these studies opted to ignore measurements from the flyby body in the 7 days leading up to and following each flyby.

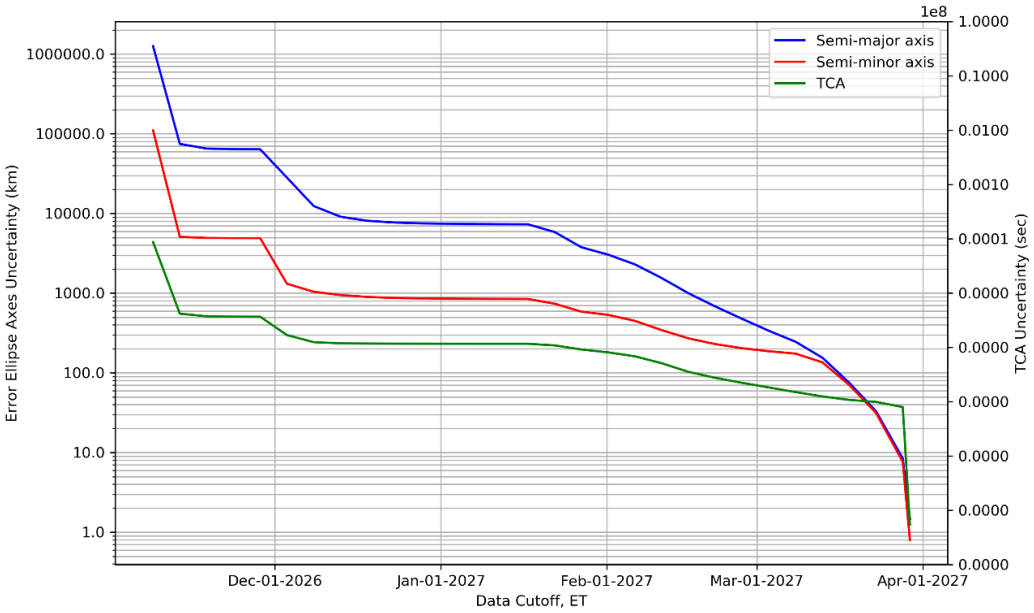

Figure 9: B-plane uncertainty at the first Venus flyby as predicted along the Earth-Venus arc

Figure 9 highlights an important circumstance resulting from the reliance on optical navigation for the Earth-Venus arc (and additional interplanetary arcs). The uncertainty associated with the prediction of the B-plane crossing conditions is quite large, up until the end of the arc and approach to Venus. Generally, very little time is given to react to an erroneous B-plane prediction, due to the prediction not being made with enough confidence to discern whether a corrective maneuver may be necessary, or if an implemented corrective maneuver produced the desired results. This corresponds with an uncertainty of the B-plane crossing conditions that may be prohibitively large too soon prior to the flyby to mitigate risk requirements. An example illustrating the Earth flyby is given below:

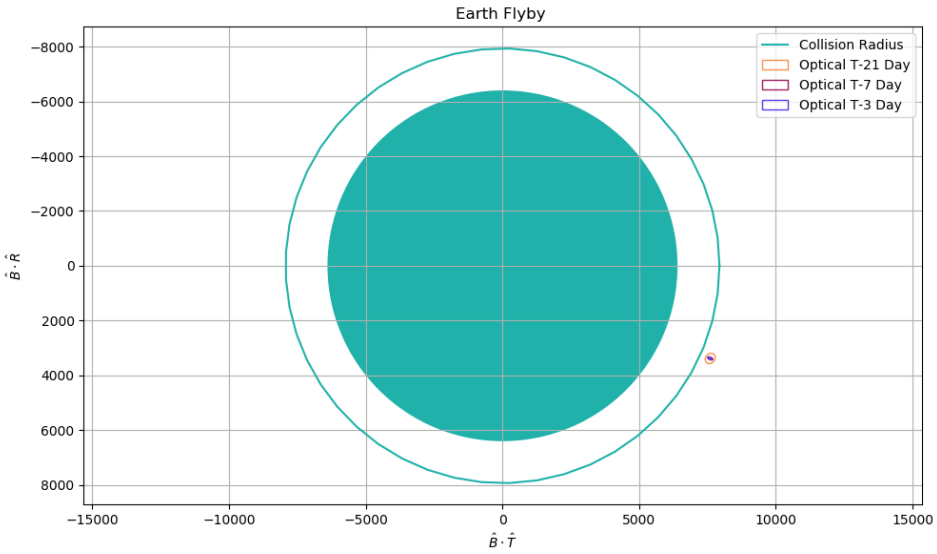

Figure 10: B-Plane predictions of Earth flyby at T-21 days, T-7 days, and T-3 days, using optical navigation only

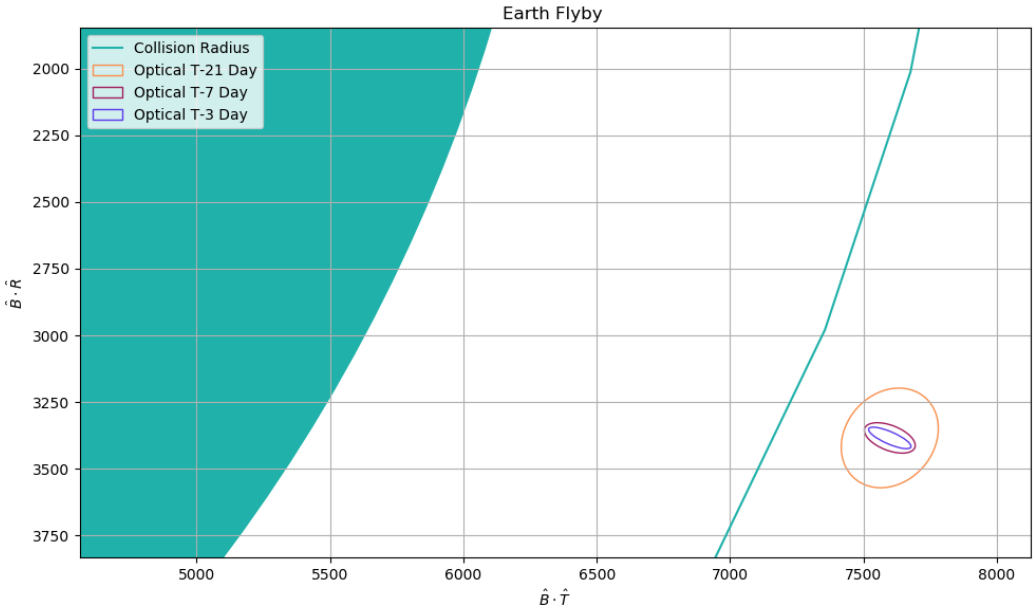

Figure 11: Zoomed depiction of B-plane predictions of Earth flyby at T-21 days, T-7 days, and T-3 days, using optical navigation

The Earth B-plane crossing conditions are known with a confidence of approximately 500 km (3-sigma) along the longest axis 21 days prior to the flyby, and it isn't until 7 days prior or even sooner where the crossing conditions are known with a more comfortable certainty. The corresponding overlap with the collision radius is not far outside of 3σ probability at T-21 days, especially in the case where a corrective maneuver must be implemented, where the corresponding increase to the velocity uncertainty due to maneuver execution errors may worsen the knowledge of the flyby conditions unless that knowledge is supplemented through other means.

Errors on the order of approximately 100km are generally permissible for deep space travel and communications purposes, but may be unsuitable for navigating a planetary flyby. From this, it may be inferred that deep-space navigation during quiescent periods of the interplanetary cruise

may be accomplished with optical navigation via measurements to planetary beacons. However, additional measurement data may be required prior to executing a planetary flyby, as the state uncertainty collapses upon approach to the flyby, but potentially too late to satisfy flyby execution and risk mitigation requirements. If flybys must be executed within some statistical bounds such that prohibitive cleanup costs are avoided, or such that probability of collision limits are not exceeded, then the predictions at mission-critical times (such as T-21 days, T-7 days, and T-3 days) produced via optical navigation alone may not be sufficiently small. The planetary flybys of the inner solar system take on much similar geometry than what is shown in Figures 10 and 11, and is also shown in subsequent figures in the *Optical Navigation Supplemented with Radiometric Observables* section, which highlights numerical representations of flyby conditions under various supplemental radiometric measurement strategies.

The Earth-Saturn leg is of special importance in this feasibility study, as the number of viewable planetary beacons decreases as their angular location relative to the Sun approaches and falls below the solar exclusion threshold of 30 degrees.

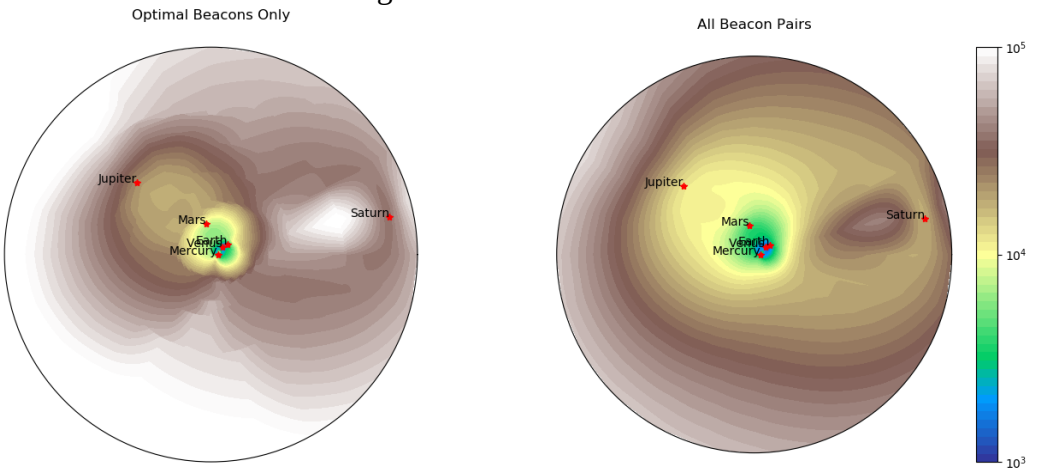

Figure 12: Expected positional uncertainties in the outer solar system, showing worsened observability outbound to Saturn.

Figure 12 illustrates this issue. The planets of the inner solar system maintain close proximity to the Sun, and observing them becomes difficult due to solar exclusion. This may be delayed, but not avoided completely with a physical baffling to allow better viewing of near-Sun bodies, but the close angular proximity of these beacons and their position relative to the spacecraft and Saturn would not provide very valuable information. Recall that optimal beacon selection prefers beacons which are close to the spacecraft and whose position vectors relative to the spacecraft create a near 90 degree angle. The situation is worsened as Jupiter also retreats behind the Sun during most of this leg, resulting in positional uncertainty on the order of several thousand kilometers inbound to Saturn. This positional uncertainty is not improved upon until reaching close proximity to Saturn, which complicates the computation, execution, and observation of mid-course corrections.

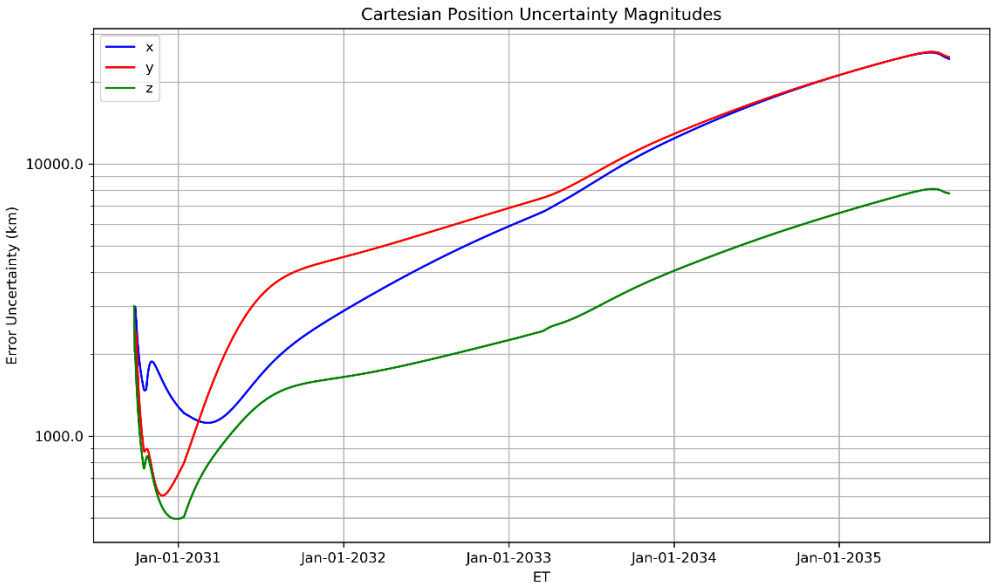

Figure 13: Instantaneous uncertainty evolution outbound to Saturn

Even without the consideration of mid-course corrections, the positional state uncertainty outbound to Saturn grows unbounded. This is due to the limited viewability of the inner planets and Jupiter, with Saturn being the only available beacon to measure right ascension and declination with respect to:

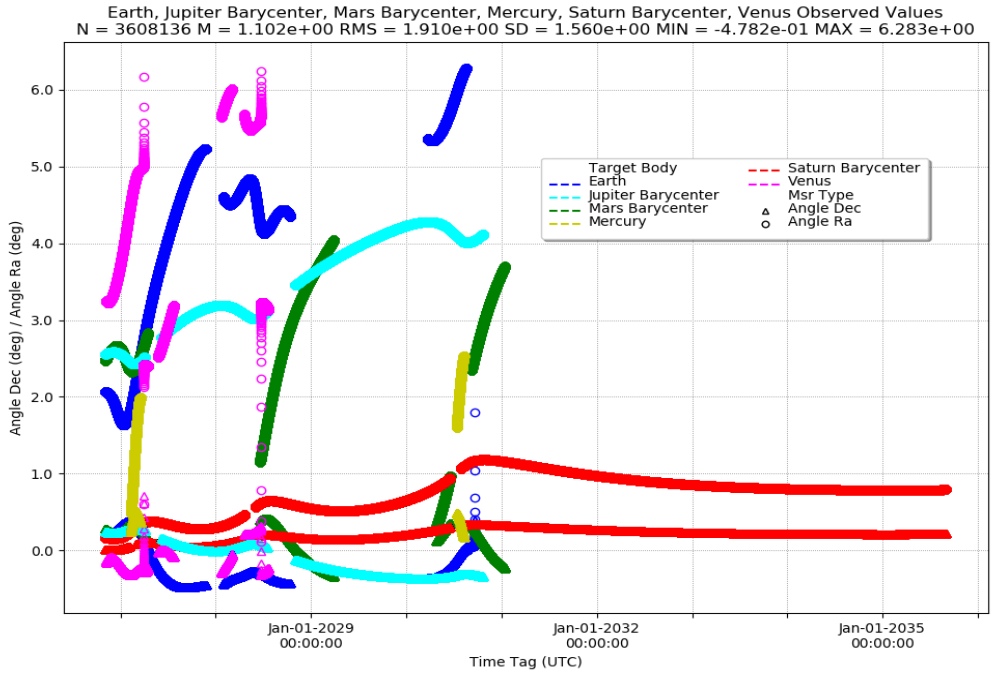

Figure 14: Collected measurements along the entire interplanetary cruise, showing a drought of measurements while outbound to Saturn

Figure 14 showcases this issue from a measurement availability perspective. Once the spacecraft is well outside the orbits of the inner planets, the only available beacon that may be measured is Saturn. The very low variability in right ascension and declination implies that the state space which may reproduce these measurements within statistical significance is quite large. Saturn is

observed to be slow-moving, and so a much larger number of spacecraft position-velocity states exist which may reproduce the measurement trajectory, resulting in worsened resolution of the flown trajectory. Calculating and executing trajectory corrections while outbound to Saturn will be done with large uncertainty, where the effects of a maneuver will be difficult to resolve, if possible at all. For this leg of the interplanetary cruise, additional measurement sources should be considered, as optical navigation does not deliver navigation uncertainties sufficient for trajectory prediction and maneuver planning. It is recommended that radiometric navigation be utilized during this leg of the cruise, and other areas on the interplanetary cruise which show sparse measurement availability. Results which support this recommendation are presented in the following section.

Optical Navigation Supplemented with Radiometric Observables

Optical-only navigation studies indicate navigation performance which may allow for safe deep-space navigation during quiescent periods of interplanetary travel within the inner solar system. Positional uncertainties on the order of hundreds of kilometers and velocity uncertainties on the order of tens of centimeters per second may be permissible during quiescent deep-space travel, as the dynamics which drive the spacecraft's trajectory are not subject to wide acceleration dispersions due to changes in position of a few hundred kilometers. Even in the presence of statistical deep-space trajectory correction maneuvers, which serve to directly contribute to a spacecraft's velocity uncertainty, optical-only navigation constrains the spacecraft's instantaneous state uncertainty such that reliable predictions may still be made about the spacecraft's future orbital state for ground-station pointing purposes.

However, close attention must be paid to the execution of planetary flybys, which are extremely sensitive to B-plane intersection conditions. A misplaced B-plane crossing may result in large corrective maneuvers, and so constraining the uncertainty of predicted B-plane crossing conditions is a mission-critical focus which warrants evaluation of supplemental navigation methods. As such, supplemental radiometric tracking is incorporated into this section of the interplanetary navigation studies. Radiometric measurements can drive planetary flyby navigation uncertainties below acceptable bounds such that navigation accuracy requirements derived in subsequent analyses may be more readily satisfied.

A configurable radiometric measurement strategy is assumed, with the following measurement configurations, each spanning a 45-day tracking interval leading up to the next planetary flyby:

Table 6: Radiometric tracking schedules and measurement noise values.

Flyby	Start Date	Flyby Date	Range Uncertainty 1σ STD	Doppler Uncertainty 1σ STD	Tracking Pass Cadence
Venus 1	12-Feb-2027	29-Mar-2027	1.0 m 10 m	0.1 mm/s 1.0 mm/s 10.0 mm/s	1/wk, 8 hours 1/wk, 4 hours 1/wk, 1 hour
Venus 2	06-May-2028	20-Jun-2028	1.0 m 10 m	0.1 mm/s 1.0 mm/s	1/wk, 8 hours 1/wk, 4 hours

				10.0 mm/s	1/wk, 1 hour
Earth 1	07-Aug-2030	21-Sep-2030	1.0 m 10 m	0.1 mm/s 1.0 mm/s 10.0 mm/s	1/wk, 8 hours 1/wk, 4 hours 1/wk, 1 hour

The intent with this study is to identify radiometric tracking schedules which supplement optical measurements to reduce the predicted B-plane uncertainty at pre-flyby epochs (21 days, 7 days, and 3 days prior) and allow for corrective maneuvers to be executed with ample time for cleanup. Assumed measurement noise values span one to two orders of magnitude to capture the sensitivity of navigation performance to ground-based tracking capabilities, the lowest measurement noise values assumed in this analysis are consistent with those assumed in navigation analyses using Deep Space Network (DSN) radiometric measurements. Uncertainty analysis results for the Earth flyby configuration is shown below. Much of the supplemental radiometric tracking results are reminiscent of these, which illustrate how various radiometric tracking cadences serve to constrain the predicted B-plane crossing conditions as predicted at the T-21 days, 7 days, and 3 days epochs.

Table 7: Predicted B-plane uncertainties for Earth flyby, made at 21 days prior to the flyby.

Optical 05 Min Cadence		**B-PLANE UNCERTAINTY AT Earth T-21 DAYS**		
Radio Measurement Strategy	**State Type**	**SMAA (km 3σ)**	**SMIA (km 3σ)**	**TCA (sec 3σ)**
No Radio	B-Plane	337.5119	186.8477	18.2412
		Radiometric Range and Doppler Noise: 1m & 0.1mm/s		
1/Week, Max 8 Hour	B-Plane	95.4024	41.0901	0.7087
1/Week, Max 4 Hour	B-Plane	122.8847	58.3409	0.7142
1/Week, Max 1 Hour	B-Plane	159.6627	145.7617	0.7584
		Radiometric Range and Doppler Noise: 1m & 1mm/s		
1/Week, Max 8 Hour	B-Plane	143.9779	72.1884	0.7194
1/Week, Max 4 Hour	B-Plane	158.1899	138.7184	0.7535
1/Week, Max 1 Hour	B-Plane	160.7256	150.0571	0.7720
		Radiometric Range and Doppler Noise: 1m & 1 cm/s		
1/Week, Max 8 Hour	B-Plane	149.8102	87.7897	0.7253
1/Week, Max 4 Hour	B-Plane	159.6817	146.9459	0.7619
1/Week, Max 1 Hour	B-Plane	160.7721	150.1584	0.7732
		Radiometric Range and Doppler Noise: 10m & 0.1mm/s		
1/Week, Max 8 Hour	B-Plane	95.6036	41.1748	0.7087
1/Week, Max 4 Hour	B-Plane	123.0034	58.4305	0.7142
1/Week, Max 1 Hour	B-Plane	159.6629	145.7630	0.7584
		Radiometric Range and Doppler Noise: 10m & 1mm/s		
1/Week, Max 8 Hour	B-Plane	151.8484	88.5264	0.7264
1/Week, Max 4 Hour	B-Plane	158.6436	141.6779	0.7563
1/Week, Max 1 Hour	B-Plane	160.7271	150.0606	0.7720
		Radiometric Range and Doppler Noise: 10m & 1 cm/s		
1/Week, Max 8 Hour	B-Plane	159.8501	146.9307	0.7659
1/Week, Max 4 Hour	B-Plane	160.6957	150.0289	0.7723
1/Week, Max 1 Hour	B-Plane	160.7784	150.3312	0.7810

With no radiometric tracking, optical navigation provides a T-21 day predicted B-plane crossing condition with uncertainties on the order of a few hundred kilometers. Supplemental radiometric tracking may provide a navigation solution which helps to reduce this flyby uncertainty by 50% or more along the longest axis, even at the most casual of measurement cadences. At T-21 days, there remains ample time to adjust the B-plane crossing conditions based on the current best state

estimate, where a corrective maneuver may still be reliably deemed necessary and executed if the desired crossing conditions lie outside statistical bounds on the current prediction.

Table 8: Predicted B-plane uncertainties for Earth flyby, made at 7 days prior to the flyby.

Optical 05 Min Cadence		B-PLANE UNCERTAINTY AT Earth T-7 DAYS		
Radio Measurement Strategy	**State Type**	**SMAA (km 3σ)**	**SMIA (km 3σ)**	**TCA (sec 3σ)**
No Radio	B-Plane	148.1775	144.4109	7.4495
		Radiometric Range and Doppler Noise: 1m & 0.1mm/s		
1/Week, Max 8 Hour	B-Plane	26.5979	13.0115	0.2035
1/Week, Max 4 Hour	B-Plane	33.0107	15.6201	0.2080
1/Week, Max 1 Hour	B-Plane	39.8254	26.8730	0.2247
		Radiometric Range and Doppler Noise: 1m & 1mm/s		
1/Week, Max 8 Hour	B-Plane	36.6469	17.1103	0.2105
1/Week, Max 4 Hour	B-Plane	39.6469	25.5256	0.2225
1/Week, Max 1 Hour	B-Plane	40.4241	37.5483	0.2453
		Radiometric Range and Doppler Noise: 1m & 1 cm/s		
1/Week, Max 8 Hour	B-Plane	37.8261	18.6955	0.2128
1/Week, Max 4 Hour	B-Plane	39.8665	30.2412	0.2286
1/Week, Max 1 Hour	B-Plane	40.6062	37.9471	0.2486
		Radiometric Range and Doppler Noise: 10m & 0.1mm/s		
1/Week, Max 8 Hour	B-Plane	26.6421	13.0187	0.2035
1/Week, Max 4 Hour	B-Plane	33.0334	15.6343	0.2080
1/Week, Max 1 Hour	B-Plane	39.8254	26.8743	0.2247
		Radiometric Range and Doppler Noise: 10m & 1mm/s		
1/Week, Max 8 Hour	B-Plane	38.2334	18.6388	0.2130
1/Week, Max 4 Hour	B-Plane	39.7305	27.1297	0.2244
1/Week, Max 1 Hour	B-Plane	40.4287	37.5612	0.2454
		Radiometric Range and Doppler Noise: 10m & 1 cm/s		
1/Week, Max 8 Hour	B-Plane	39.9880	32.5303	0.2312
1/Week, Max 4 Hour	B-Plane	40.4235	37.4820	0.2451
1/Week, Max 1 Hour	B-Plane	40.6217	37.9673	0.2491

Similar to the T-21 day prediction, radiometric tracking serves to more tightly constrain the predicted B-plane crossing conditions. Even 7 days prior, certain measurement cadences allow for the safe execution of a planetary flyby under the predicted uncertainties shown above, still allowing for fine tuning of the flyby conditions with 7 days to react. Additionally, supplemental radiometric tracking at T-21 days serves to perform nearly as good or better than the optical navigation solution at T-7 days, allowing for two weeks or more of planning and reaction time for trajectory correction.

Table 9: Predicted B-plane uncertainties for Earth flyby, made at 3 days prior to the flyby.

Optical 05 Min Cadence		B-PLANE UNCERTAINTY AT Earth T-3 DAYS		
Radio Measurement Strategy	**State Type**	**SMAA**	**SMIA**	**TCA**
No Radio	B-Plane	83.3317	82.4386	7.208
		Radiometric Range and Doppler Noise: 1m & 0.1mm/s		
1/Week, Max 8 Hour	B-Plane	10.0489	5.5976	0.0708
1/Week, Max 4 Hour	B-Plane	15.0334	8.4850	0.0751
1/Week, Max 1 Hour	B-Plane	19.4706	17.1562	0.0981
		Radiometric Range and Doppler Noise: 1m & 1mm/s		

1/Week, Max 8 Hour	B-Plane	17.4783	10.5950	0.0803
1/Week, Max 4 Hour	B-Plane	19.4516	16.6317	0.0965
1/Week, Max 1 Hour	B-Plane	19.8386	18.8321	0.1032
		Radiometric Range and Doppler Noise: 1m & 1 cm/s		
1/Week, Max 8 Hour	B-Plane	18.1157	12.0337	0.0834
1/Week, Max 4 Hour	B-Plane	19.6273	17.8483	0.1000
1/Week, Max 1 Hour	B-Plane	19.8548	18.8677	0.1035
		Radiometric Range and Doppler Noise: 10m & 0.1mm/s		
1/Week, Max 8 Hour	B-Plane	10.0851	5.6095	0.0708
1/Week, Max 4 Hour	B-Plane	15.0497	8.4976	0.0751
1/Week, Max 1 Hour	B-Plane	19.4706	17.1565	0.0981
		Radiometric Range and Doppler Noise: 10m & 1mm/s		
1/Week, Max 8 Hour	B-Plane	18.7515	12.4415	0.0851
1/Week, Max 4 Hour	B-Plane	19.5383	17.0856	0.0978
1/Week, Max 1 Hour	B-Plane	19.8391	18.8334	0.1032
		Radiometric Range and Doppler Noise: 10m & 1 cm/s		
1/Week, Max 8 Hour	B-Plane	19.7129	18.1709	0.1004
1/Week, Max 4 Hour	B-Plane	19.8384	18.8321	0.1032
1/Week, Max 1 Hour	B-Plane	19.8607	18.8906	0.1059

In each case, even in most casual radiometric tracking cadences, the supplemental radiometric tracking allows for an estimation uncertainty of the B-plane crossing conditions of less than half that provided by optical navigation. In the most extreme cases, the predicted B-plane crossing conditions are known to a fidelity as high as four times more precise than with no radiometric tracking at all. As the flyby approaches optical measurements relative to the flyby planet serve to further constrain the B-plane predictions, as the motion of the spacecraft relative to the flyby body is more readily observable over a shorter time. This results in a situation where the flyby conditions may be known well via optical navigation, but usually only in cases where the flyby is soon to happen. These circumstances are especially important when considering low altitude flybys, as is the case with the first Venus flyby shown below:

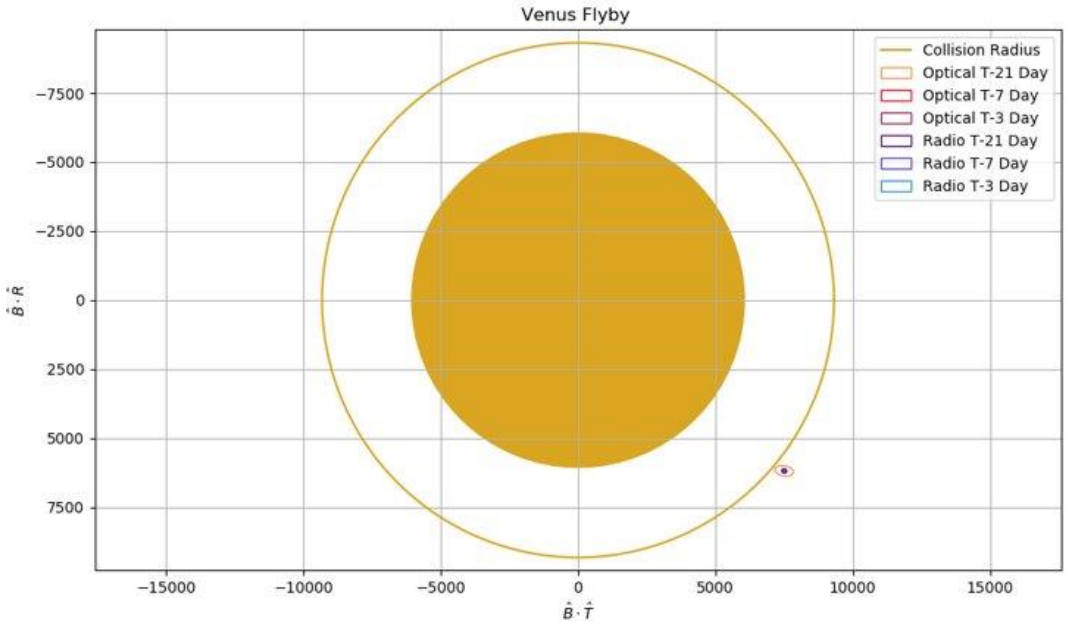

Figure 15: Predicted B-plane crossing conditions for the first Venus flyby, with optical-only and radio-supplemented tracking, at T-21 day, 7 day, and 3 day pre-flyby epochs

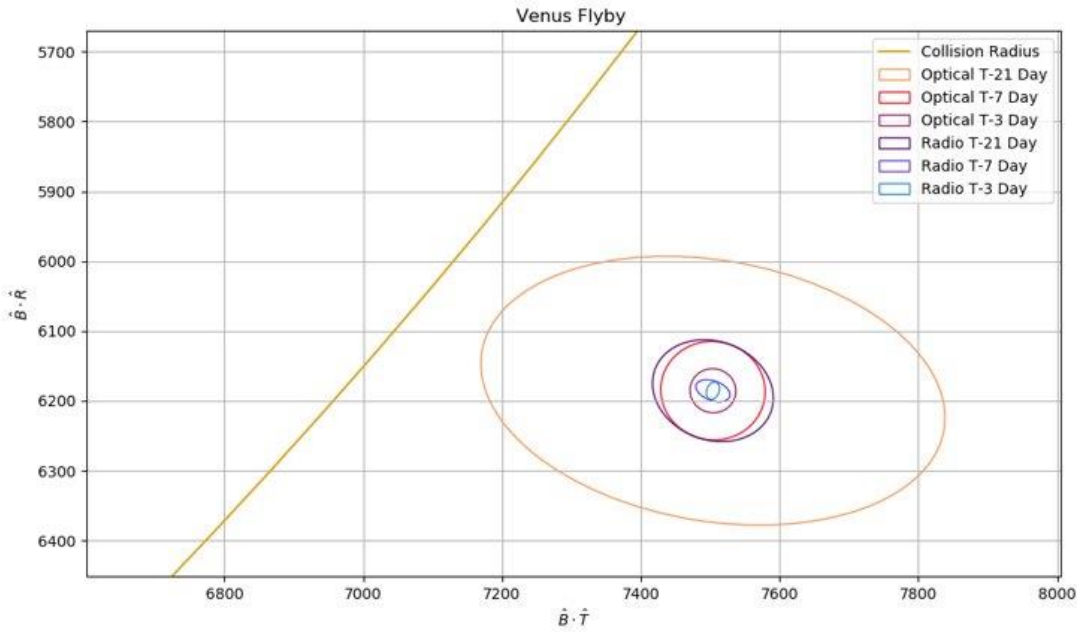

Figure 16: Zoomed depiction of the predicted state uncertainties at the B-plane crossing, relative to the Venus impact radius projected onto the B-plane

Figure 15 and Figure 16 above depict the predicted B-plane crossing conditions for the first Venus flyby, relative to the impact radius of Venus projected onto the B-plane. A spacecraft flying by Venus with the planned relative velocity must not cross the B-plane within the impact radius, as a collision or interaction with the upper atmosphere may result at periapsis or sooner. Figure 2 shows that at 21 days prior to the flyby, optical-only navigation results predict that an interaction with the collision radius is not far outside the 3-sigma probability, while supplemental radiometric tracking serves to reduce that likelihood to less than 6-sigma. Additionally, optical-only navigation of the flyby could require that the spacecraft correct for more than 300km across the B-plane at T-21 days. Any corrections to the trajectory shall inject uncertainty into knowledge of the spacecraft's velocity, worsening the knowledge of the B-plane crossing and requiring additional measurement information to constrain the estimate of the upcoming flyby.

Optical-only navigation may allow for the safe execution of planetary flybys under circumstances which allow a spacecraft to react accurately on short notice, on the order of 7 to 14 days, and have fuel margins to correct for navigation uncertainties near this magnitude, as well as to correct the trajectory for any errors resulting from executing an imperfect flyby under the uncertainties shown above. These conditions illustrate that navigating planetary flybys with optical-only navigation may impose mission risks and cost which must be accepted or addressed with mitigation strategies. Radiometric tracking can dramatically reduce the likelihood of navigation-related mission risk where optical navigation does not suffice, and at a minimum, is a recommended supplement during mission-critical events such as flybys and maneuver execution.

Saturn Moon Tour Studies

Optical-only Navigation

The Saturnian moon tour officially starts upon Saturn orbit insertion (SOI), and navigation analysis of the moon tour trajectories is conducted on an arc-by-arc basis. Each arc is considered independently, where optical measurements of the Saturnian satellites are used to generate a new trajectory solution and prediction of the next B-plane crossing conditions for the upcoming moon flyby. The moon tour start and end dates are as follows:

Table 10: Start and end dates of each tour in the Saturn moon tour.

Moon Tour	Start Date	End Date
Titan	15-NOV-2035 04:15:04 TDB	30-JAN-2037 15:15:05 TDB
Rhea	30-JAN-2037 15:15:05 TDB	18-OCT-2038 22:44:01 TDB
Dione	18-OCT-2038 22:44:01 TDB	20-MAY-2039 12:32:32 TDB
Tethys	20-MAY-2039 12:32:32 TDB	07-DEC-2039 07:50:43 TDB
Enceladus	07-DEC-2039 07:50:43 TDB	15-DEC-2039 10:01:59 TDB

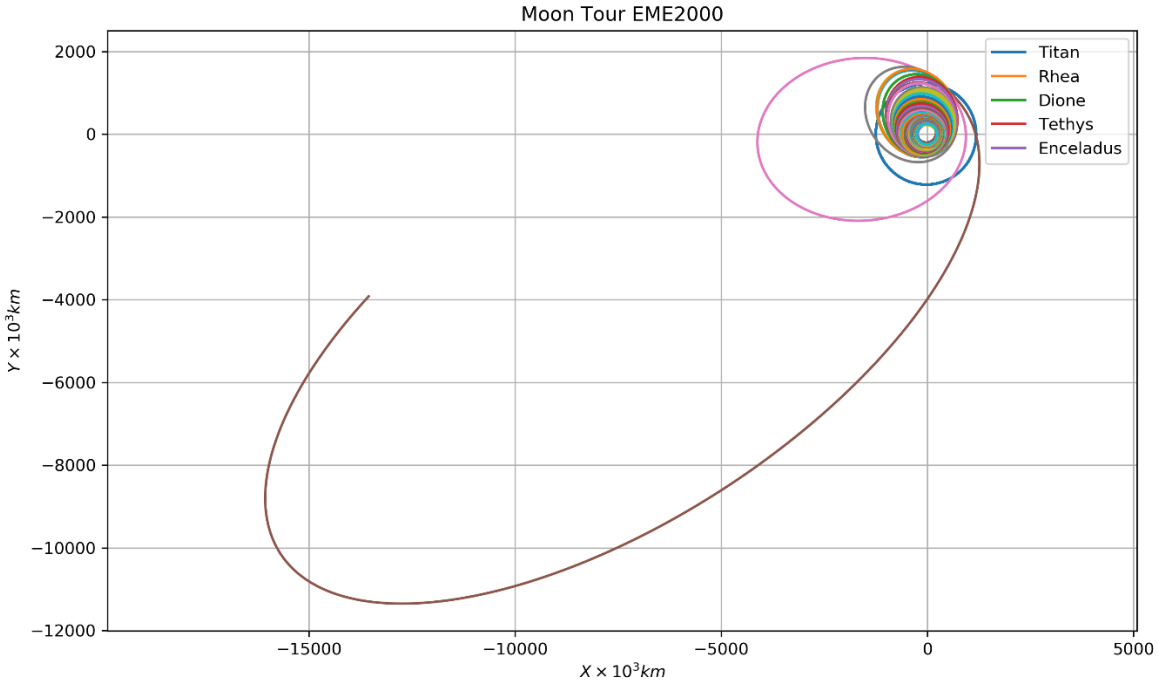

Figure 17: Saturnian moon tour trajectory

The trajectories and maneuver design which result from the mission design efforts are ingested into the moon tour analysis framework. Right ascension and declination measurements are collected with respect to the Saturnian moons: Titan, Rhea, Dione, Tethys, and Enceladus. These measurements are used to understand how the spacecraft's position-velocity state may be estimated and to what fidelity the spacecraft's state may be known.

Like the interplanetary tour, beacon-relative right ascension and declination measurements are used to analyze the spacecraft's state uncertainty. A useful circumstance resulting from collecting these measurements when in orbit around Saturn, is that the faster relative motion of the spacecraft and moons with respect to each other serves to further constrain the space of possible trajectories of best-fit, moreso than during interplanetary legs of the outbound EVVES trajectory, where the motion of the measurement beacons (being the planets) are not as distinguishable over short time periods.

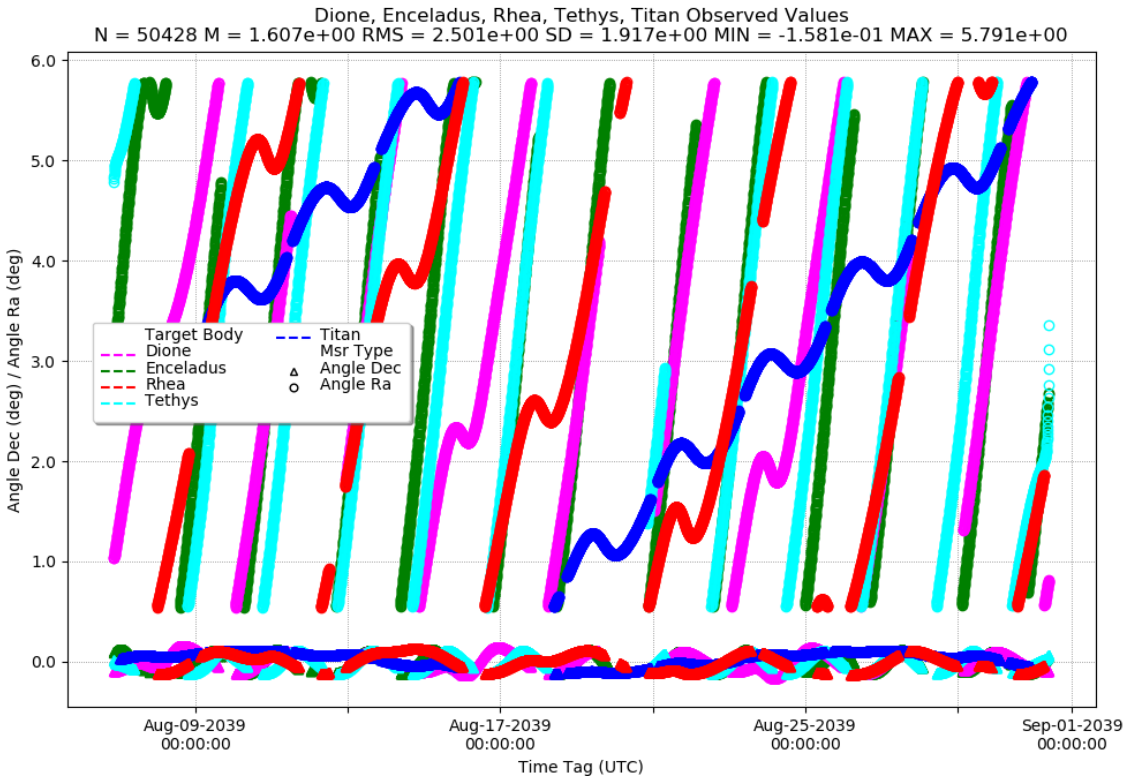

Figure 18: Sample Right Ascension and Declination Measurements for one of the Tethys tour legs

The enhanced motion of the spacecraft with respect to the moons and the wide variation in measurements allows for the estimation schema to more tightly constrain the state estimate of the spacecraft, as there exists a smaller state space of trajectories which may reproduce the observed measurements within statistical significance. This stands in stark contrast to Figure 6, where the rate of change of the right ascension and declination of the planetary beacons is slow, and may take months to show a considerable change. This measurement methodology is used to evaluate the navigation performance on each leg of the moon tour, and also informs when the Saturnian system may provide a richer source of measurements than the planetary beacons while inbound to SOI.

Generally, navigation solutions improve in quality as the successive flybys and orbit reductions serve to decrease the size of the spacecraft's orbit around Saturn, shortening its orbital period and increasing the time rate of change of the right ascension and declination observables of the Saturnian satellites.

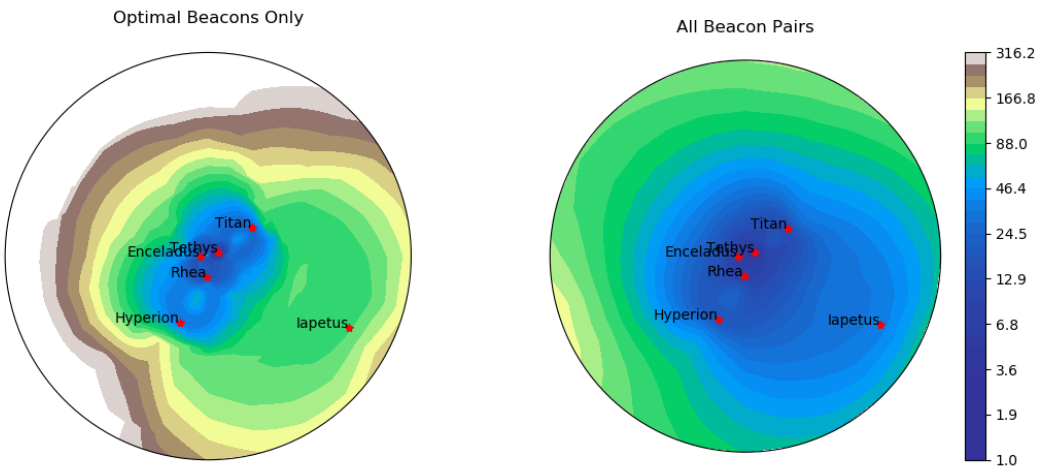

Figure 19: 1-sigma variance of spacecraft positional state uncertainty under measurement configurations which include only the optimal pair of beacons (left) and all available beacons (right).

Figure 19 illustrates the expected positional state uncertainty which can be gleaned from observing only the optimal pair of Saturnian beacons or all available beacons as a function of location within the Saturnian system at a single point in time. A significant takeaway from this cursory glance is that the state solutions improve dramatically as the spacecraft flies interior to Titan's orbit. This marks a significant improvement upon the interplanetary optical navigation strategy, where the Saturnian system offers a significant improvement on navigation accuracy, dropping under 10 kilometer variance in several key locations, even under circumstances where only two of the available beacons are observed.

Subsequent analysis investigates the performance of this navigation strategy over time, where maneuvers, flybys, and other perturbations serve to affect the knowledge of the spacecraft's position-velocity state. Similar to the analysis of the interplanetary cruise, it is pivotal to constrain the prediction of the subsequent flyby conditions such that corrective maneuvers may be applied to clean up errors from the previous flyby or maneuver execution errors en-route to the next flyby. This presents a unique problem, where the higher-quality state solution that optical navigation within the Saturnian system offers must also be achieved over significantly shorter time intervals, some spanning fewer than 72 hours.

Covariance analysis along each leg of the moon tour typically falls within two categories: one in which the spacecraft has very little time to discern its own position and velocity before coordinating the next flyby, and the other in which the spacecraft's state estimate reaches a steady state long before the upcoming flyby, where predictions of the uncertainty of upcoming B-plane crossing conditions is hindered most by dynamical uncertainty and time to the next flyby. Visual examples of these conditions are provided in the figures below.

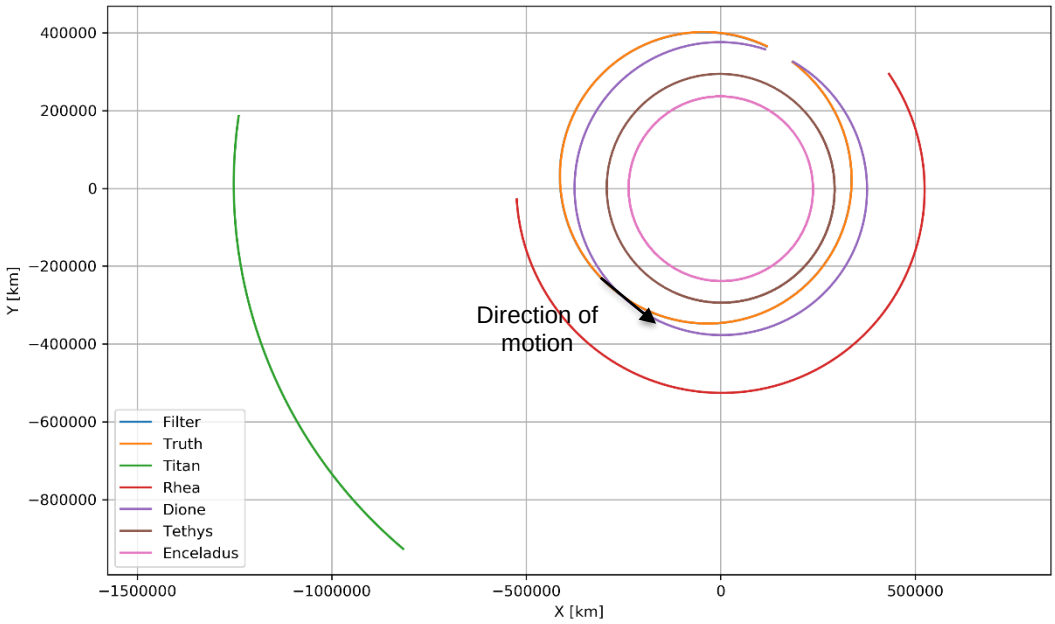

Figure 20: Orbit visualization of a two-day arclength between Dione flybys.

This single flyby arc in the Dione tour spans only one Dione revolution about Saturn, where the spacecraft has fewer than three days to constrain its post-flyby state and make a prediction of the upcoming B-plane crossing conditions for the next flyby. This presents a conflict between the amount of measurement data which may be collected and the time until the next flyby, which is a departure from the multi-revolution approach which allows for multiple revolutions about Saturn prior to the next Dione encounter.

Single revolution (or single-rev) resonant orbit flybys impose the most stringent navigation requirements, where a spacecraft may be required to generate a sufficient navigation solution and coordinate a maneuver in fewer than 24 hours prior to an upcoming flyby. Conversely, this may impose a requirement on acceptable mission risk, which requires less precise knowledge of the upcoming flyby prior to planning and executing corrective maneuvers, the performance of which may not be known accurately until after the flyby has concluded.

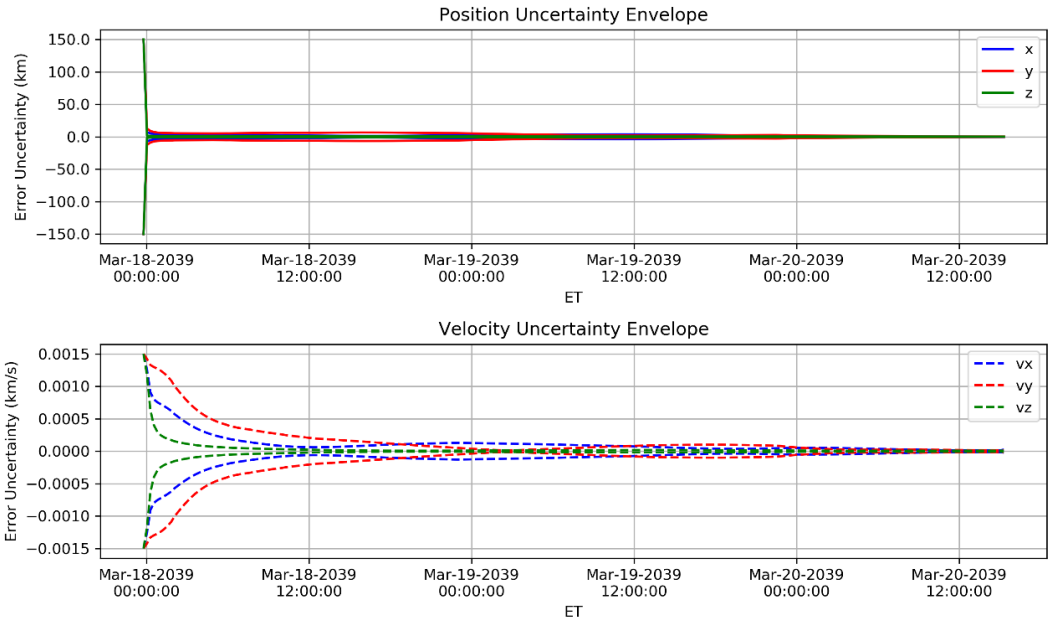

Figure 21: Position and velocity uncertainty envelopes for a two-day arclength between Dione flybys.

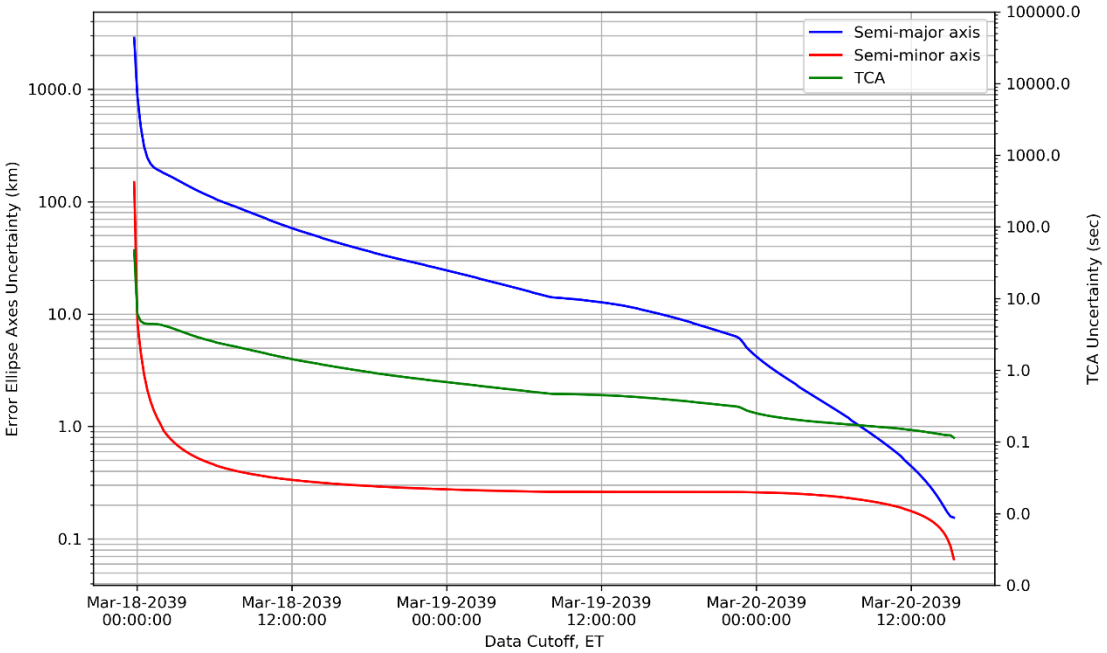

Figure 22: B-Plane uncertainty predictions for a two-day arclength between Dione flybys.

Figure 21 and Figure 22 further illustrate the conflict at hand, where the instantaneous state uncertainty has not reached a steady state, and the B-plane crossing conditions for the next Dione flyby are not known below a 10 km fidelity along the largest axis until fewer than 24 hours prior to the upcoming flyby. This presents a navigation challenge, where necessary adjustments to the B-plane crossing conditions may be difficult to discern and implement soon enough before the flyby to safely navigate it as intended. The bounds on permissible flyby execution errors may be defined in a physical sense, permitting a close approach no lower than some altitude or a probability of collision no higher than some upper boundary. Additionally, permissible flyby

execution errors may be found via permissible fuel margins, where each flyby must be executed within statistical bounds outside of which cleanup maneuvers become too costly.

Below, an example of a multi-rev arc is given, showcasing navigation performance when the spacecraft is allowed ample time to reach a steady-state uncertainty, where the additional information yielded from subsequent measurements balances with dynamical uncertainties:

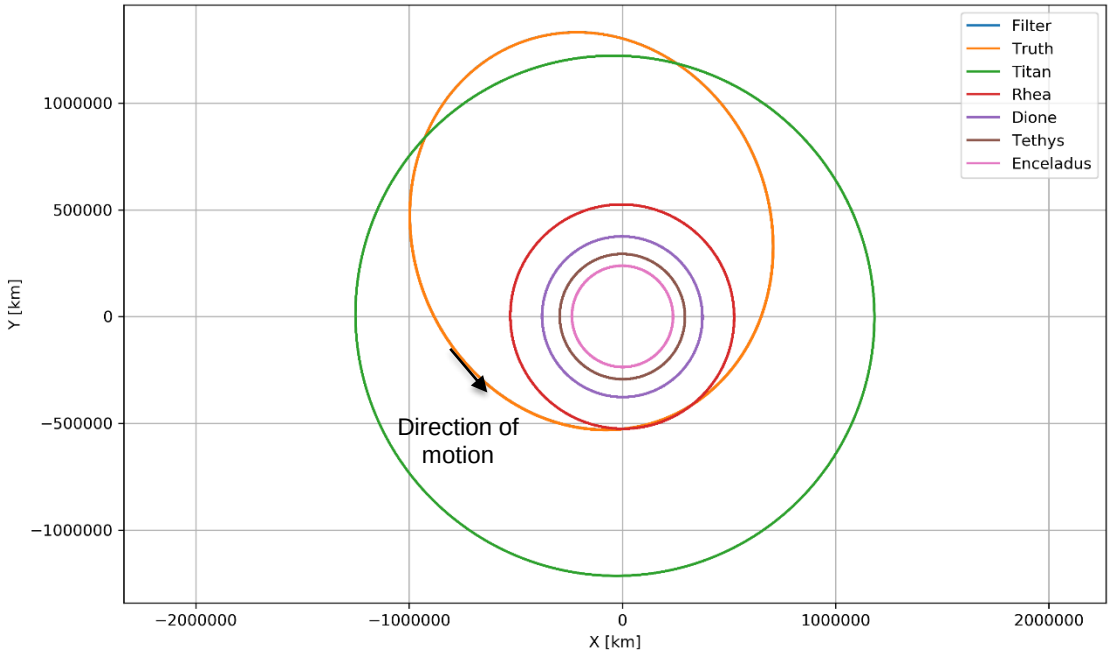

Figure 23: Orbit visualization of a multi-rev arc between Rhea flybys in Saturn-centered inertial frame.

Here, the spacecraft is allowed multiple revolutions about Saturn prior to the upcoming Rhea flyby, where all Saturnian satellites trace out their full orbital paths at least once. During this multiple revolution case, the spacecraft constrains its position and velocity state estimates to a saturated size, balancing between measurement information, measurement cadence, and dynamical uncertainty. In this case, the spacecraft's state uncertainty reaches a size which is maintained by incoming measurement information, and the largest hindrance to the knowledge of the upcoming flyby conditions results from dynamical effects worsening the confidence of the predictions far into the future.

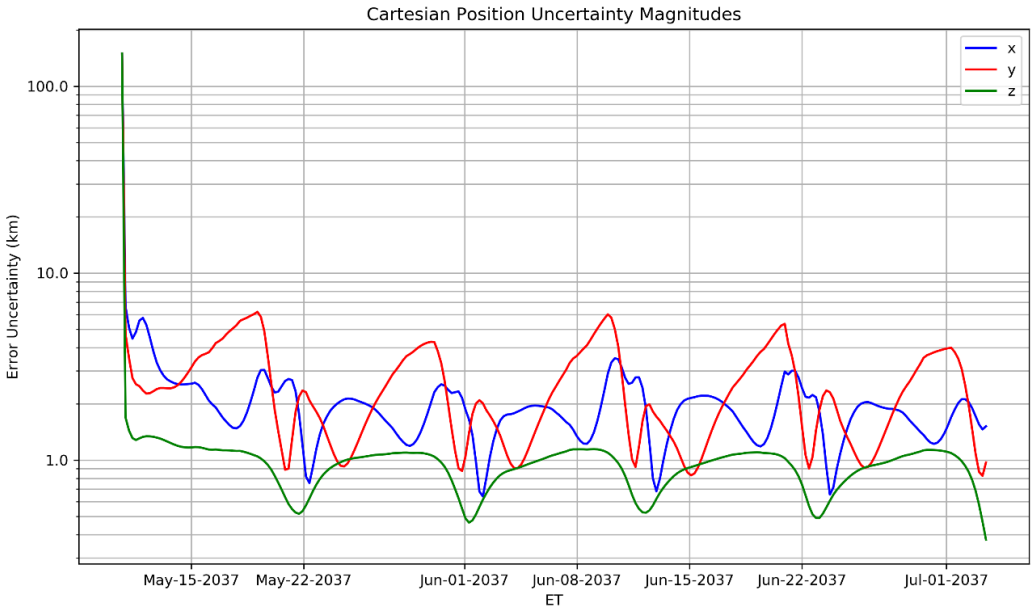

Figure 24: Positional uncertainty components displayed on a log axis, illustrating the steady-state uncertainty behavior.

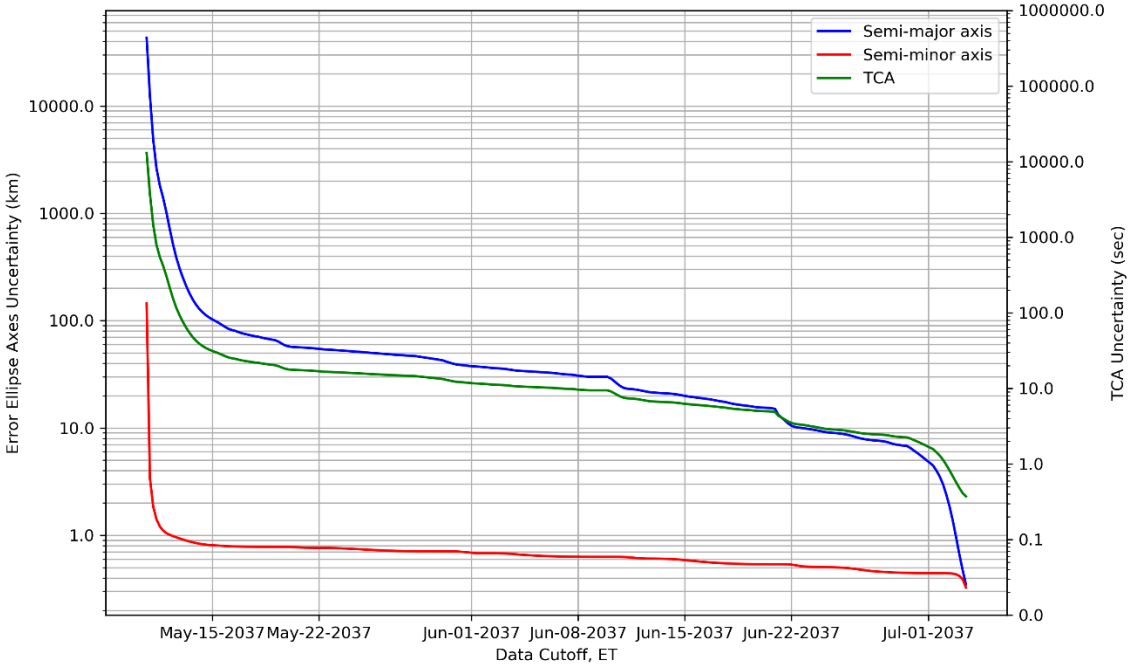

Figure 25: B-plane uncertainty predictions made along the multi-rev arc between Rhea flybys.

Figure 24 illustrates the difference between single-rev and multi-rev cases. Here, the spacecraft is able to reduce its state uncertainty to a point where it is no longer decreasing in size, and instead the collected measurements serve to maintain a consistent mean (though oscillating) state uncertainty for the remainder of the arc. Upon reaching this steady state, the subsequent B-plane predictions shown in Figure 25 illustrate the time-to-flyby behavior mentioned previously, where although predictions are made with a similarly sized initial uncertainty, the predictions made with a shorter time-to-flyby result in higher confidence predictions of the B-plane crossing conditions. In this case, the flyby conditions are known to a fidelity of 10 km 3-sigma approximately 11 days

prior to the flyby, yielding ample time for corrective maneuvers to be calculated, implemented, and observed.

Below, an overview of each flyby in the moon tour is given, with the initial epoch of Jan 28th, 2036 corresponding to the periapsis raising maneuver which targets the first Titan encounter. All subsequent arc begin times correspond to post-flyby conditions, and arc end times correspond with the upcoming flyby date. Durations are reported which represent how much time is left until the upcoming flyby where the B-plane crossing conditions are known to a fidelity of 10 km 3-sigma along the longest uncertainty axis, noted as the 10-km Time-To-Flyby condition.

Table 11: Moon tour flybys, their arc lengths, and time before the next flyby which results in a 10km 3-sigma B-Plane uncertainty.

Flyby Body	Arc Begin	Arc End (Flyby Date)	Arc Length (days)	Maneuver (m/s)	10-km Time-To-Flyby (days)
Titan	28-JAN-2036 09:21:18.5570	18-NOV-2036 06:17:36.6134	294.87	None	-2.36
Titan	18-NOV-2036 12:17:36.6134	05-JAN-2037 01:18:32.4873	47.542	None	-3.04
Titan	05-JAN-2037 07:18:32.4873	20-JAN-2037 23:26:20.9963	15.672	None	-3.32
Rhea	20-JAN-2037 23:26:20.9963	13-MAR-2037 03:45:37.0463	50.752	46.138	-4.03
Rhea	13-MAR-2037 09:45:37.0463	18-APR-2037 07:33:15.4295	35.908	105.58	-5.17
Rhea	18-APR-2037 13:33:15.4295	10-MAY-2037 10:32:09.1856	21.874	42.049	-10.9
Rhea	10-MAY-2037 16:32:09.1856	03-JUL-2037 16:19:33.4374	53.991	None	-10.8
Rhea	03-JUL-2037 22:19:33.4374	13-AUG-2037 21:09:24.4262	40.951	None	-9.66
Rhea	14-AUG-2037 03:09:24.4262	02-OCT-2037 14:03:22.5593	49.454	None	-6.13
Rhea	02-OCT-2037 20:03:22.5593	20-OCT-2037 15:10:18.8574	17.796	84.771	-17.2
Rhea	20-OCT-2037 21:10:18.8574	08-DEC-2037 13:36:46.0840	48.685	118.81	-8.18
Rhea	08-DEC-2037 19:36:46.0840	31-JAN-2038 18:54:50.1564	53.97	None	-7.98
Rhea	01-FEB-2038 00:54:50.1564	08-MAR-2038 22:09:00.3337	35.884	None	-8.04
Rhea	09-MAR-2038 04:09:00.3337	22-MAR-2038 11:22:29.8055	13.301	None	-7.13
Rhea	22-MAR-2038 17:22:29.8055	23-APR-2038 02:20:17.8132	31.373	None	-7.15
Rhea	23-APR-2038 08:20:17.8132	11-MAY-2038 04:26:18.4643	17.837	None	-7.63
Rhea	11-MAY-2038 10:26:18.4643	02-JUN-2038 19:21:41.6947	22.371	None	-7.07
Rhea	03-JUN-2038 01:21:41.6947	04-JUL-2038 10:37:55.3854	31.386	None	-9.54
Rhea	04-JUL-2038 16:37:55.3854	27-AUG-2038 16:04:08.0177	53.976	None	-9.5
Rhea	27-AUG-2038 22:04:08.0177	21-SEP-2038 17:15:46.8743	24.799	None	-10.1
Rhea	21-SEP-2038 23:15:46.8743	26-SEP-2038 05:52:26.0824	4.2754	None	-1.26
Rhea	26-SEP-2038 11:52:26.0824	07-OCT-2038 00:30:12.2816	10.526	53.566 m/s	-4.8
Dione	07-OCT-2038 00:30:12.2816	16-NOV-2038 19:49:51.4018	40.805	40.884 m/s	-12.4
Dione	16-NOV-2038 21:49:51.4018	28-NOV-2038 05:16:12.5743	11.309	95.099 m/s	-7.82
Dione	28-NOV-2038 07:16:12.5743	22-DEC-2038 20:42:08.1377	24.559	None	-11.1
Dione	22-DEC-2038 22:42:08.1377	05-JAN-2039 13:22:36.3443	13.611	None	-9.53
Dione	05-JAN-2039 15:22:36.3443	22-JAN-2039 00:02:49.3183	16.361	None	-9.75
Dione	22-JAN-2039 02:02:49.3183	12-FEB-2039 21:24:07.9059	21.806	None	-10.1
Dione	12-FEB-2039 23:24:07.9059	13-MAR-2039 22:44:22.5626	28.972	17.569	-9.62
Dione	14-MAR-2039 00:44:22.5626	17-MAR-2039 21:46:26.8327	3.8764	None	-1.89
Dione	17-MAR-2039 23:46:26.8327	20-MAR-2039 15:34:08.0270	2.6581	None	-0.957
Dione	20-MAR-2039 17:34:08.0270	24-MAR-2039 09:17:27.9827	3.655	None	-2.44
Dione	24-MAR-2039 11:17:27.9827	20-APR-2039 18:00:34.4044	27.279	None	-10
Tethys	20-APR-2039 18:00:34.4044	19-MAY-2039 12:50:11.7279	28.693	251.77	-12.4
Tethys	19-MAY-2039 13:20:11.7279	09-JUN-2039 07:24:02.4739	20.752	None	-7.42
Tethys	09-JUN-2039 07:54:02.4739	20-JUN-2039 15:17:47.4760	11.308	None	-8.81

Tethys	20-JUN-2039 15:47:47.4760	03-JUL-2039 20:26:06.5725	13.193	None	-11
Tethys	03-JUL-2039 20:56:06.5725	18-JUL-2039 23:06:09.3213	15.09	None	-13.5
Tethys	18-JUL-2039 23:36:09.3213	06-AUG-2039 20:24:13.5206	18.866	None	-7.66
Tethys	06-AUG-2039 20:54:13.5206	31-AUG-2039 09:17:50.0384	24.516	None	-9.64
Tethys	31-AUG-2039 09:47:50.0384	28-SEP-2039 16:58:18.3171	28.298	7.2187	-0.338
Tethys	28-SEP-2039 17:28:18.3171	01-OCT-2039 10:18:35.3310	2.7015	47.833	-0.0324
Tethys	01-OCT-2039 10:48:35.3310	03-OCT-2039 08:40:03.5690	1.9107	93.991	-0.286
Tethys	03-OCT-2039 09:10:03.5690	05-OCT-2039 22:59:08.4253	2.5757	5.1582	-2.16
Tethys	05-OCT-2039 23:29:08.4253	31-OCT-2039 18:55:26.4488	25.809	None	-11
Tethys	31-OCT-2039 19:25:26.4488	19-NOV-2039 15:58:00.9504	18.855	None	-12.1
Enceladus	19-NOV-2039 15:58:00.9504	07-DEC-2039 06:25:38.6556	17.6025	None	-6.24
Enceladus	07-DEC-2039 06:55:38.6556	15-DEC-2039 10:01:59.4454	8.1294	17.700	-7.29
Enceladus	15-DEC-2039 10:31:59.4454	02-JAN-2040 08:09:12.6817	17.9	None	-10.7
Enceladus	02-JAN-2040 08:39:12.6817	11-JAN-2040 22:18:21.0454	9.5688	None	-7.94
Enceladus	11-JAN-2040 22:48:21.0454	01-FEB-2040 11:32:57.5561	20.53	15.594	-14.9
Enceladus	01-FEB-2040 12:02:57.5561	12-FEB-2040 10:57:32.5553	10.954	None	-9.87
Enceladus	12-FEB-2040 11:27:32.5553	06-MAR-2040 13:27:27.3241	23.083	4.6667	-11.1
Enceladus	06-MAR-2040 13:57:27.3241	18-MAR-2040 21:40:29.6093	12.321	None	-10.2
Enceladus	18-MAR-2040 22:10:29.6093	13-APR-2040 23:07:27.2455	26.039	None	-16.8
Enceladus	13-APR-2040 23:37:27.2455	27-APR-2040 16:34:08.8147	13.706	10.015	-11.6
Enceladus	27-APR-2040 17:04:08.8147	12-MAY-2040 18:26:59.0600	15.057	7.7737	-10.1
Enceladus	12-MAY-2040 18:56:59.0600	29-MAY-2040 08:31:51.7667	16.565	0.7695	-10.7
Enceladus	29-MAY-2040 09:01:51.7667	08-JUN-2040 01:24:29.9662	9.6823	12.977	-4.72

Table 11 presents a cohesive overview of each flyby in the delivered moon tour trajectory, presenting the arc durations between flybys, and the time prior to the next flyby at which the knowledge of the upcoming flyby conditions are known to a fidelity smaller than 10 kilometers 3-sigma along the largest axis. Generally, all flybys are known to a fidelity of 10 km or smaller at some point prior to the flyby, with variability in the 10-km time-to-flyby knowledge that spans several weeks down to as few as a couple of hours.

These conditions are motivated by a few factors, most namely being available beacons to measure right ascension and declination with respect to (the exact number varies due to Saturn occultations and solar exclusion constraints), maneuvers being present in the flyby arcs, maneuver magnitudes, and maneuver execution time prior to the flyby. Maneuvers found during mission design efforts are placed with optimality conditions in mind, and although the placement of maneuvers is chosen in part to minimize maneuver magnitude, placement soon before a flyby may inhibit the knowledge of flyby conditions to prohibitively short timespans, as is the case with the Tethys tour. Maneuver execution errors are considered in this covariance analysis so as to worsen the knowledge of the spacecraft's velocity post-maneuver, where additional measurement data is required to constrain the spacecraft's state uncertainty and subsequently constrain the uncertainty of the upcoming B-plane crossing prediction. These maneuver execution errors are considered to be 1% 1-sigma.

This analysis highlights a few key areas during the moon tour where additional measurement information may be required. During the Titan moon tour, the measurement geometry resulting from the spacecraft flying at altitudes well above the Saturnian satellites that it takes measurements with respect to results in poorer state knowledge, where the upcoming flyby conditions are not well known until the spacecraft approaches Titan for the upcoming flyby. Additionally, short-

duration measurement arcs seen in the Dione and Tethys tours require the spacecraft to discern its flight path in just a few days, where any necessary corrections to the trajectory must be discerned and implemented soon before the flyby with little time to react. This is especially true for the Tethys tour, where several large maneuvers between flybys are conducted, with each arc only spanning just a few days. This may be more manageable if data arcs spanned multiple flybys as more data could be used to plan each flyby, though there may be some drawbacks to fitting through multiple dynamical events which could be detrimental to filter performance. Then again, these drawbacks are generally more evident for low flybys of planets and the effect is likely less prominent for flybys of the Saturnian moons. In any case, this has not been studied and would require more analysis to evaluate feasibility.

For cases where the 10-km time-to-flyby duration is quite low (Titan moon tour, and a few short-duration arcs during the Dione and Tethys tours), supplemental radiometric navigation may be leaned upon to reduce the risk of navigating a flyby with low knowledge of the upcoming flyby conditions. Radiometric tracking stands as a recommended means to mitigate poor knowledge of upcoming flybys, but remains to be analyzed from a ground-station accessibility perspective, where access to radiometric measurements during very specific time periods (such as low time-duration arcs between moon flybys) would be required to safely navigate. Increasing the confidence with which a flyby is conducted may serve to decrease the fuel margins allocated for correcting imperfectly executed flybys, where a poorly flown flyby may require more fuel to be allocated for cleanup. Risk mitigation in the form of larger fuel margins could be more costly in those cases. This is especially true for flybys of Titan, which significantly change the spacecraft's trajectory, and accurately achieving the flyby targets is considerably more important.

Enceladus Orbit Navigation

Occultation Timing Measurement Model

During the Science phase, star occultation timing measurements are under consideration to substitute radiometric navigation. These timing measurements produce a time tag associated with a star's appearance or disappearance over a body's horizon. For orbit determination processing, these measurements are proxied as the star's line of sight (LOS) height above the occulting body's surface. The LOS height mitigates non-linearity difficulties in the Kalman filter as time is an independent variable in the filter model [7].

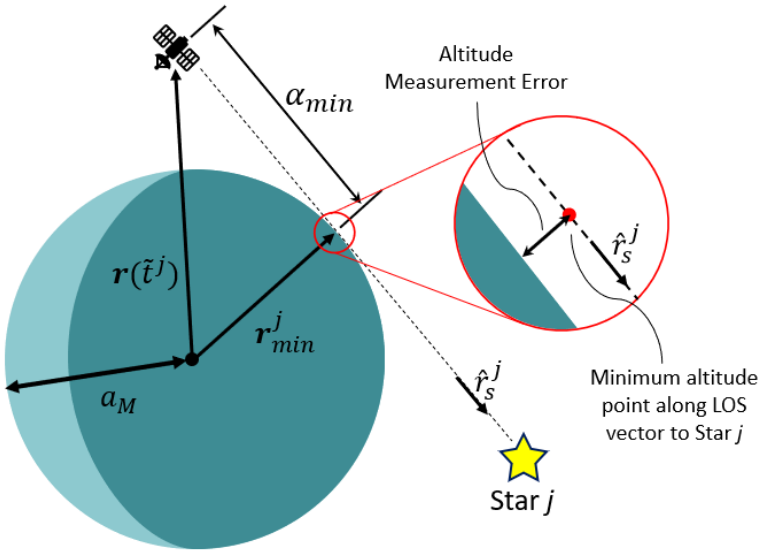

Figure 26: Diagram of the occultation timing measurement model. The observed "altitude" of a star rise or set differs from the predicted altitude at the same epoch by the altitude measurement error. Adapted from [7].

The observed LOS height is always zero at the time of the detected occultation. If the orbit solution is inaccurate, the computed LOS height is non-zero. As the orbit determination solution is iterated, the computed LOS height approaches zero. Unlike [7], Advanced Space simulates Enceladus as an ellipsoid rather than a sphere. The ellipsoid has the following semi-axis lengths: 256.6 km x 251.4 km x 248.3 km [8]. The equation used for LOS height in [7] are not valid for an ellipsoid, so the following equations are used to accommodate the ellipsoidal shape.

$$h_{LOS} = \left|\boldsymbol{r}_{LOS,surface}\right| \bullet sin\left(\angle \hat{\boldsymbol{r}}_{\boldsymbol{s}}^{\boldsymbol{j}}\, \boldsymbol{r}_{LOS,surface}\right)$$

$$\alpha_{min} = \sqrt{\left|r_{SC,surface}\right|^2 - h_{LOS}^2}$$

h_{LOS} is the minimum altitude of the star's LOS above the planet. $r_{SC,\,surface}$ is the vector from the spacecraft to the surface point closest to the LOS. The equations above are derived using the fact that the LOS vector and point on the ellipsoid surface forms a plane. Inside this plane, the distance from the surface point to the LOS forms a 90 degree angle which allows for a right triangle to be formulated and the above equations to be used.

The LOS height measurement uncertainty calculations are from [6] and accounts for uncertainty in the body topography, uncertainty in the star catalog, and uncertainty in measurement timing.

$$\sigma_j = \sqrt{\sigma_h^2 + \left(\alpha_{min}\sigma_s^j\right)^2 + \left(\dot{h}_{min}^j \sigma_{tj}\right)^2}$$

$\sigma_j$is the one sigma uncertainty associated with the h_{LOS} measurement type. σ_h corresponds to the topographic radial uncertainty which for Enceladus is assumed to be 57 meters [9]. σ_s^j is the

uncertainty in the star catalog in the axial direction. σ_{tj} is the uncertainty due to timing. This consists of two different uncertainties: clock resolution, and time differences due to diffraction.

$$\sigma_{tdiff} = \frac{|\boldsymbol{r}^j_{min}|\sqrt{\lambda_{light}\alpha_{min}}}{(\boldsymbol{r}^j_{min})^T \mathbf{v}(\tilde{\boldsymbol{t}}^j)}$$

λ_{light} is the wavelength of the star in Angstroms. For the Enceladus simulation, the wavelength for stars was assumed to be 5000 Angstroms, 2 arc seconds of star catalog uncertainty [10] and clock resolution of 0.001 seconds. For the Enceladus simulation and current assumptions, the dominant uncertainty is from the topographic map. The other uncertainties accounted for < 1 meter for a simulation starting in a 270.1 x 290.1 km polar orbit.

Occultation Timing Navigation Results

The occultation timing measurement has the potential to provide many measurements as stars set and rise over the horizon of a low-altitude orbit. In particular, the motion of the spacecraft results in many observations in the spacecraft velocity (transverse) and anti-velocity directions. As such, spacecraft state uncertainty can be well constrained in this direction. However, because measurements taken directly "forward" or "backward" largely only provide information in this direction, the measurement type mainly reduces velocity- and radial-direction uncertainty. Uncertainty in the orbit-normal direction is mostly unaffected by the information provided from measurements oriented in the velocity direction. Figure 27 illustrates this well. Star occultation measurements taken in the velocity direction are many and informative for spacecraft state. Orbit normal uncertainty is mostly unaffected here.

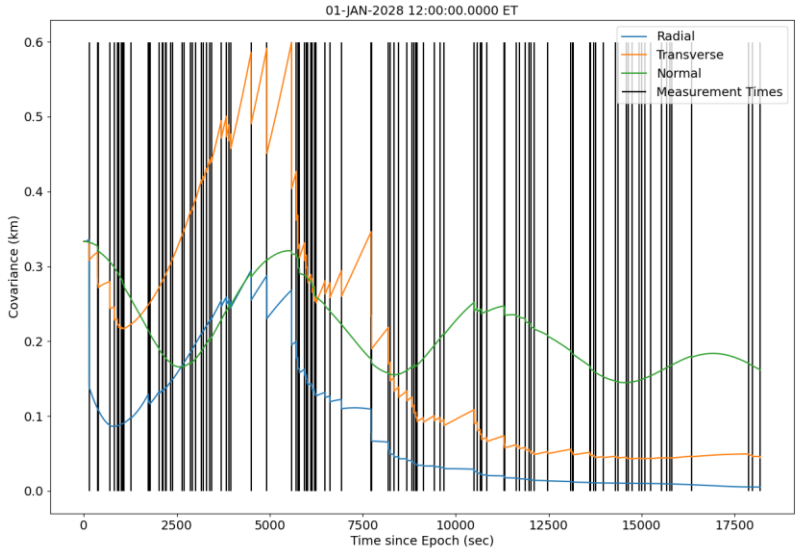

Figure 27: Transverse, normal, and radial state uncertainties using star occultations in the purely in the orbit velocity direction.

Figure 28 shows state uncertainty instead for measurements taken purely in the orbit normal direction. While velocity, radial, and orbit-normal uncertainty can be aided by these measurements, star occultations are much less frequent. It can be helpful to visualize this scenario by imagining looking out the front and side windows of a moving car. Looking out the front window, objects rise over the horizon more often than do when looking out the side windows. The same is true for this measurement type. Looking out the side window of the car is analogous to taking measurements purely in the orbit-normal direction of the spacecraft's trajectory.

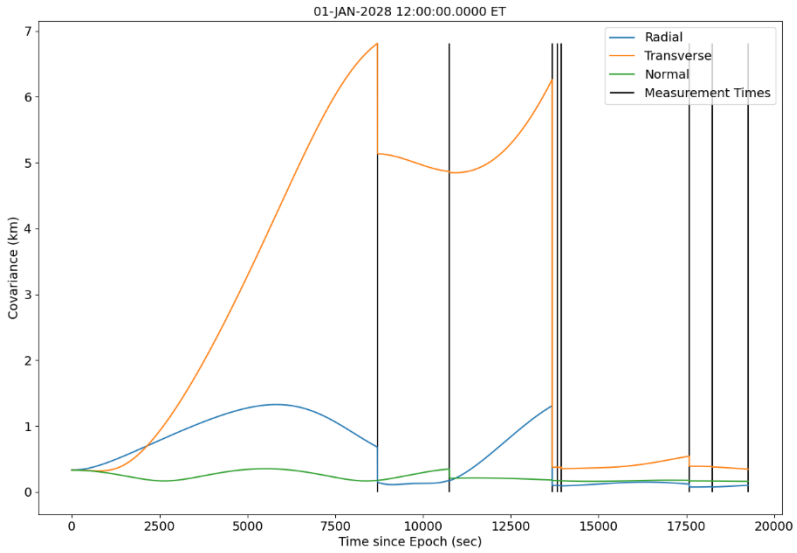

Figure 28: Transverse, normal, and radial state uncertainties using star occultations in the purely in the orbit normal direction.

The figures above help inform how the availability of measurements impacts spacecraft state uncertainty with this measurement type. Noting that star occultation measurements assume a dark limb of the center body, when accounting for the 33 hour orbital period of Enceladus combined with the orientation (and drift) of the spacecraft's orbit, it cannot be guaranteed that measurements will be oriented both in the velocity direction and towards the shaded side of Enceladus. While occultation timing measurements can be promising for some points in time, it may require supplemental navigation observables to provide steady state uncertainty throughout the science phase of the mission. Classic line of sight optical navigation utilizing Saturn's moons as beacons can be a valuable source of information as shown previously in this report, and the availability of beacons is dependent on the relative motion of the moons and the Sun, rather the spacecraft and Enceladus (barring occultations from Enceladus, which are unlikely to constrain viewability of all beacons at once.)

Conclusion

The analyses provided here present a broad analysis of each phase of an interplanetary mission to Enceladus primarily utilizing optical navigation observables and limited radiometric tracking. The optical navigation strategy serves to constrain spacecraft uncertainty during much of the trajectory. Especially during quiescent periods, optical navigation in the interplanetary phase can maintain

spacecraft state uncertainty on the order of 100 km and 1 m/s 3σ. Modelling deterministic deep space maneuvers and stochastic trajectory correction maneuvers during these deep space periods inflates state uncertainty according to expected maneuver execution errors, but optical navigation still serves to bound and decrease uncertainty post-maneuver, given there is ample time to observe the change in velocity. The steady-state uncertainty during quiescent periods supports optical navigation as a feasible navigation strategy for these periods. However, leading up to critical events such as interplanetary flybys, optical navigation seems insufficient to properly constrain uncertainty to the level required to target and correct for relatively low-altitude, sensitive flyby targets. Figure 16 illustrates optical navigation capabilities as compared to optical navigation supplemented with radiometric tracking and indicates that even limited tracking in the weeks leading up to and following flybys can greatly improve knowledge and control of B-plane crossings. One significant caveat for optical navigation in the interplanetary cruise is the final leg outbound to Saturn where the inner Solar System planets become gradually less valuable and eventually unusable as they become obscured by their proximity to the Sun. At this distance from the Sun, the only potentially available targets are Saturn and Jupiter, but Jupiter is also obscured by its Sun angle by coincidence. In this case, for this mission, uncertainty grows unbounded until arrival at the Saturn system. There may be an opportunity to use Jupiter's trojan asteroids, which reside in the Sun-Jupiter L4 and L5 stability points and therefor would not be constrained by the Sun angle constraint imposed on Jupiter itself. It should be noted, though, that most asteroids are relatively small, their brightness properties are less predictable due their irregular shape, and their distance from the spacecraft and relatively high ephemeris uncertainty translates small angular errors into much larger state uncertainty than closer beacons are. The main focus to improve feasibility of the interplanetary trajectory using optical navigation should be this final outbound leg to Saturn which remains the weak point from a navigation perspective.

The Saturn moon tour benefits from a variety of close, fast-moving beacons which greatly constrain spacecraft state uncertainty when compared to the interplanetary phase. However, like the final leg of the interplanetary trajectory, the first injection maneuver into the Saturn system places the spacecraft on a large orbit whose apoapsis is still relatively distant from the Saturn system. This limits the usability of the Saturnian moons due to the spacecraft's distance from them and their close angular proximity. Special attention should be given to this phase of the trajectory to support navigation. Additionally, this analysis makes no effort to simulate viewability or image processing limitations due to the presence of Saturn's rings. A thorough vetting of these constraints is necessary to fully validate an optical navigation strategy in the Saturn system. One last limitation of the moon tour analysis is the frequency of moon flybys and deep space maneuvers. Table 11 details the navigation performance between successive flybys during the moon tour. Most legs between flybys are sufficiently long and contain sufficiently few maneuvers to constrain state uncertainty leading into the next flyby. However, many legs suffer from shorter tracking arcs, on the order of a handful of days, and include large deep space maneuvers. This results in significantly higher state uncertainty at the subsequent flyby and higher mission risk. Additional measurement observables would be needed for these legs of the moon tour such as radiometric or other novel optical navigation measurements. One measurement type of interest utilizes the sunlit limbs of rocky bodies observed during a flyby to measure the spacecraft's relative position to the body [11]. Initial results using this measurement strategy are promising for pre- and post-flyby navigation, however the measurement implementation is still under development at Advanced Space and has not been included officially for this analysis.

Navigation in the Enceladus science orbit can be managed using optical strategies with some caveats. Occultation timing measurements serve to constrain the in-track uncertainty of the spacecraft's orbit due to a wealth of measurements originating in this direction as the spacecraft passes over Enceladus' horizon. It's not guaranteed, however, that the dark side of Enceladus is in the velocity or anti-velocity direction of the spacecraft's motion. When the spacecraft's orbit places available measurements mostly in the orbit-normal direction, instances of star-rise and star-set are much sparser, limiting this strategy's ability to constrain state uncertainty. Classic line of sight (LOS) optical navigation using Saturn's moons are still available in the science orbit, albeit somewhat more constrained due to occultations by Enceladus, however the limitations described for the Moon tour still apply here. Finally, frequent station keeping maneuvers are required to maintain a science orbit that meets mission objectives. The station keeping maneuvers are expected to cost approximately 1 m/s per day for the duration of the science phase. The uncertainty contributed by these burns has not been adequately modelled and should be made a point of emphasis for future analysis.

A final phase of the mission which has not been covered explicitly in the mission design or navigation analyses is the final downlink orbit for the spacecraft. This orbit should be quiescent and is meant to allow for the downlink of requested science data. This is likely a Saturn-centered orbit with similar size as Enceladus' orbit. In accordance with the optical navigation results from the Saturn moon tour, this final phase of the mission could be supported by the LOS optical navigation strategy used in the moon tour phase. Additionally, given the lack of ongoing maneuver planning during this mission phase, the navigation requirements can likely be far less stringent than other phases of the mission – the primary goal of the navigation is to maintain an accurate enough estimate for Earth pointing.

The work here provides a broad overview of potential navigation strategies which may be used for the mission. While many areas of the trajectory could be supported by an optical navigation strategy, many areas remain which require more in-depth analysis. In particular: the final interplanetary leg outbound to Saturn is limited by the ability to view beacons. The initial arrival orbit at Saturn poses a similar challenge, where the spacecraft is unable to utilize the Saturn system or Solar System bodies for navigation. During the moon tour, frequent flybys and deep space maneuvers often hurt spacecraft state uncertainty more than LOS optical navigation can maintain it. Further analysis is also required to ensure that optical navigation can support frequent station keeping maneuvers during the science and downlink phases of the mission. However, the results of this feasibility study indicate that optical navigation is not sufficient as a stand-alone navigation strategy and fails to deliver a satisfactory navigation solution for mission-critical events. Radiometric tracking is recommended as a supplement, to drive down navigation errors and to decrease the likelihood of navigation-related failures, but stands to be verified from a measurement availability perspective. Deriving navigation error tolerances requires additional analysis, although those assumed in this analysis suffice as an approximate realistic target which the assumed radiometric tracking strategy (DSN tracking) satisfies, if ground-station scheduling allows.

Preliminary navigation analyses can serve as a first look at the capabilities of a given navigation strategy under a-priori assumptions provided from mission design. However, navigation must ultimately support other aspects of the mission, and estimates of expected state uncertainty cannot

stand on their own. To fully evaluate the efficacy of this navigation strategy, it must be iteratively improved alongside the trajectory design to determine whether the mission still closes. Navigation uncertainty contributes directly to maneuver design errors and subsequent correction costs. Effects of state uncertainty on maneuver design errors are often nonlinear and are not the sole contributors to maneuver cleanup costs. A thorough analysis of the flow between maneuver and navigation often involves a Monte Carlo simulation to fully account for potential sources of error and verify that navigation performs well enough such that it isn't a driving mechanism in increasing fuel costs. In addition to delving deeper into individual weak points of the navigation strategy, a direct feedback and analysis loop between mission design and navigation must be established to fully evaluate the risks involved in using this navigation strategy.

References

[1] Smith, J., Drain, T., Bhaskaran, S., and Martin-Mur, T. J. "MONTE for Orbit Determination." *International Symposium on Space Flight Dynamics*, 2017.

[2] Vallado, D. A. *Fundamentals of Astrodynamics*. Microcosm Press, Hawthorne, CA, 2013.

[3] Kennedy, B. "Deep Space 1 Navigation: Primary Mission." *Deep Space …*, 2004, p. 15.

[4] Broschart, S. B., Bradley, N., and Bhaskaran, S. "Kinematic Approximation of Position Accuracy Achieved Using Optical Observations of Distant Asteroids." *Journal of Spacecraft and Rockets*, Vol. 56, No. 5, 2019, pp. 1383–1392. https://doi.org/10.2514/1.A34354.

[5] Franzese, V., and Topputo, F. "Optimal Beacons Selection for Deep-Space Optical Navigation." *The Journal of the Astronautical Sciences*, 2020, pp. 1775–1792. https://doi.org/10.1007/s40295-020-00242-z.

[6] Walker, F. T. F. A. R. "Deep-Space Optical Navigation for M-ARGO Mission." 2021.

[7] Psiaki, M. L., Hinks, J. C., and Introduction, I. "Occultation Measurements." No. August, 2007, pp. 1–14.

[8] Archinal, B. A., Acton, C. H., A'Hearn, M. F., Conrad, A., Consolmagno, G. J., Duxbury, T., Hestroffer, D., Hilton, J. L., Kirk, R. L., Klioner, S. A., McCarthy, D., Meech, K., Oberst, J., Ping, J., Seidelmann, P. K., Tholen, D. J., Thomas, P. C., and Williams, I. P. "Report of the IAU Working Group on Cartographic Coordinates and Rotational Elements: 2015." *Celestial Mechanics and Dynamical Astronomy*, Vol. 130, No. 3, 2018. https://doi.org/10.1007/s10569-017-9805-5.

[9] Bland, M. T., Weller, L. A., Mayer, D. P., and Archinal, B. A. "A Global Shape Model for Saturn's Moon Enceladus from a Dense Photogrammetric Control Network." *ISPRS Annals of the Photogrammetry, Remote Sensing and Spatial Information Sciences*, Vol. 5, No. 3, 2020, pp. 579–586. https://doi.org/10.5194/isprs-Annals-V-3-2020-579-2020.

[10] Deutsch, E. W. "Empirical Uncertainty Estimators for Astrometry from Digital Databases." *The Astronomical Journal*, Vol. 118, No. 4, 1999, pp. 1882–1887. https://doi.org/10.1086/301044.

[11] Christian, J. A. "A Tutorial on Horizon-Based Optical Navigation and Attitude Determination with Space Imaging Systems." *IEEE Access*, Vol. 9, 2021, pp. 19819–19853. https://doi.org/10.1109/ACCESS.2021.3051914.